XFEM crack growth virtual monitoring in self-sensing CNT reinforced polymer nanocomposite plates using ANSYS

L. Rodríguez-Tembleque[*1], J. Vargas[1], E. García-Macías[2], F. C. Buroni[1], A. Sáez[1]

[1] *Escuela Técnica Superior de Ingeniería, Universidad de Sevilla, Camino de los Descubrimientos s/n, Sevilla 41092, Spain.*

[2] *Escuela Técnica Superior de Ingeniería de Caminos, Canales y Puertos, Universidad de Granada, Campus Universitario de Fuentenueva, Granada 18071, Spain.*

Abstract

This paper presents an eXtended Finite Element Method (XFEM)-based numerical scheme to compute electrical resistivity changes caused by the presence of cracks and the crack growth. Using the commercial finite element package ANSYS, the virtual continuous monitoring of the structure is solved in two steps. First, the strain response of the cracked composite domain is computed by means of the XFEM. In the second step, the electrical conductivity of the piezorresistive elements located in the domain are updated according to the strain state and the electric resistance between two electrodes of the damaged plate is computed. The comparison with the electric resistance measured for the undamaged plate allows us to detect the presence of a crack and its severity. Moreover, the crack growth process can be also monitored via the electric resistance increments. Several numerical studies are provided to show the capabilities of this computational framework.

Key words: Crack growth, XFEM, Crack detection, Damage identification, Nanocomposites.

Highlights

- Implementation of an electro-mechanical computational fracture mechanics framework for crack-growth simulation in carbon nanotube reinforced composites (CNTRC), using the commercial software ANSYS.
- Computational scheme that accounts for both the mechanical and piezoresistive behavior of cracked CNTRC: X-FEM addresses the mechanical behavior of the CNTRC whilst piezoresistive finite elements are employed to model the electrical behavior.
- Correlation study between crack growth and changes in the electrical resistance of the structure.
- Influence of crack-defects in the sensor performance.
- Virtual monitoring and sensing of structural integrity via electromechanical modelling of piezoresistive nanocomposites.

1. Introduction

Carbon NanoTube (CNT) reinforced composite (CNTRC) materials are receiving enormous attention from the scientific and engineering communities in recent years. Following the widespread in CNT research that started during

[*]corresponding author

Email address: luisroteso@us.es (L. Rodríguez-Tembleque[1])

the early 1990s and the subsequent investigations on its potential industrial applications, CNT production capacity has increased exponentially in later years and the advances in CNT synthesis and functionalization have allowed its effective use in many fields, ranging from the biomedical or automotive industries to aerospace applications [1–5].

From a mechanical point of view, numerous studies reveal how the addition of small quantities of CNT to polymers or precursor resins leads to a significant increase in the stiffness and strength of the resulting CNTRC. Furthermore, fracture toughness and fatigue performance of the CNTRC also improves without compromising other mechanical properties. For instance, Gojny et al. [6] reported relevant improvements of strength (+10%), stiffness (+15%) and fracture toughness (+43%) when adding 0.5 *wt*% of amino-functionalized Double-Walled CNTs to an epoxy matrix. Similarly, Hsieh et al. [7] observed how the addition of 0.5 *wt*% of Multi-Walled CNTs (MWCNTs) to a thermosetting epoxy polymer increased the measured fracture energy from 133 to 223 J/m^2, whilst the threshold strain-energy release rate also increased from 24 J/m^2 to 73 J/m^2. The review paper by Domun et al. [8] collects many of the available data prior to 2015- reporting the improvement on the mechanical properties of nanomaterial toughened composites.

Furthermore, CNTs are electrically conductive fillers that have the ability to confer to the polymeric CNTRC with conductive properties that, otherwise, would be absent in the neat matrix. CNTs take advantage of their large aspect ratio to form percolative-type conducting networks, all of it at low CNT concentrations [9]. For instance, the review work by Bauhofer and Kovacs [10] reports maximum conductivities of $10,000$ S/m for PMMA containing 10 *wt*% treated SWCNT, while conductivities up to 100 S/m were observed for a polyethylene matrix doped with 1 *wt*% MWCNT. In this manner, the resulting electrically conductive networks induce a piezoresistive behavior on the CNTRC. Such enabled strain self-sensing capability entails this new class of composites as good candidates for their use in Structural Health Monitoring (SHM) applications. Many studies are scattered in the scientific literature that take advantage of this feature, from cement- to polymer-based composites [11–18]. Of course, enhancement of the electro-mechanical properties of the CNTRC depends on several key factors, like the type of CNT, their alignment, achieving a homogeneous dispersion, the CNT aspect ratio or the CNT interfacial interaction with the matrix, to mention a few. Along these lines, recent advances in fabrication techniques are oriented towards ensuring the scalability and sensing repeatability of such CNTRC, so that they become a real alternative for SHM.

At any event, research efforts have not only focused on manufacturing processes, but also on developing reliable numerical simulation tools that assist in predicting the electro-mechanical behavior and the failure of CNTRC components during their service life. In the literature, several numerical approaches permit to simulate crack-type defects in composites. However, within the context of CNTRC for SHM, it is crucial that those methods allow anticipating: (i) how the presence of cracks (and their growth) will affect the CNTRC structural integrity from a mechanical point of view-; and (ii) how such presence will modify its sensor electrical resistivity- capabilities. This will be precisely the main objective of the paper: developing a computational framework to simulate numerically crack growth in CNTRC. To this end, the eXtended Finite Element Method (XFEM) [19–21], as implemented in the commercial finite element analysis software ANSYS [22], will be used in conjunction with the coupled-field piezoresistive and electrostatic elements available in the ANSYS element library. The XFEM extends the conventional finite element method to account for cracks, based on the concept of partition of unity. Basically, this technique enriches the degrees of freedom in the model with additional displacement functions that account for the jump in displacements across the crack discontinuity. In this way, cracks can be modeled in XFEM without explicitly meshing the crack surfaces and it further allows for arbitrary crack growth within the existing mesh, without the necessity of remeshing.

Although previous works have applied XFEM for fracture analysis in CNTRC, they have focused on simulating the mechanical problem, but have not tackled the effect of crack growth on the electrical conductivity of self-sensing CNTRC polymer plates. For instance, Joshi et al. [23] analyzed the effects of tensile loading on crack propagation in CNTRC using X-FEM together with contour integral technique to evaluate the stress intensity factor and J integral. Eftekhari et al. [24] developed an XFEM-multiscale approach to investigate the mechanical properties and fracture behavior of carbon nanotube (CNT)-reinforced concrete. Sahoo et al. [25] proposed an XFEM-based scheme to evaluate the effective elastic properties of 3-D full five-directional braided composites. More recently, Negi et al. [26] utilized the XFEM to conduct the study of crack growth in a thin rectangular plate containing an edge crack and a center crack and, subsequently, extended their approach to analyze the effect of additional defects in the form of voids and inclusions in the material [27]. Liu et al. [28] investigated the mechanical behavior and extra-strengthening and elongation increase mechanisms of CNT/Al-Cu-Mg nanocomposites with the aid of high-resolution digital image correlation (DIC) and XFEM. Ebrahimi [29] developed new enrichment functions for CNTRC, using a new local finite element characteristic equation for multi-material orthotropic composite domains. For stationary cracks, the authors

analyzed in a previous work [30] the crack-induced electrical resistivity changes in CNTRC by implementing a dual Boundary Element formulation combined with a finite differences scheme.

On the other hand, Shindo and coworkers realized several studies using the classical FEM displacement-based formulation, as implemented in the commercial finite element code ANSYS, to analyze the behavior of cracked CNTRC and further conducted the experimental validation of the results [31–34]. In Kuronuma et al. [31], the authors presented results for tensile tests on single-edge cracked plate specimens of CNT/polycarbonate composites, aimed at estimating the critical loads for fracture instabilities, and further conducted elasticplastic finite element simulations of the tests to evaluate the J-integrals corresponding to the experimentally determined critical loads. Later, Kuronuma et al. [32] generalized this study to analyze the fatigue crack growth response of CNT/polycarbonate composites. While these works just focused on the mechanical response of cracked CNT-based polymer composites, subsequent papers tackled also their electrical resistance behavior [33, 34]. Shindo et al. presented in [33] the results of tensile tests performed on single-edge cracked plate specimens of CNT/polymer composites, where the electrical resistance change of the specimens was monitored. As in references [31] and [32], numerical simulation using ANSYS was conducted to numerically replicate the obtained experimental mechanical results, whilst to simulate the electrical behavior of the cracked specimen, the authors developed and analytical model based on the definition of effective conductive pathways that directly related the change in the composite specimen electrical resistance to the crack extension and geometrical features of the specimen. In this manner, the electrical problem is not solved using FEM, but substituting the results of the mechanical FEM simulation (crack extension) into the proposed analytical formula, with good correlation between the experimental and numerical results. These approach was later extended by Takeda et al. [34] to mixed-mode I/II loading.

A recent review paper by Yadav et al. [35] summarizes some of the previous contributions in the scientific literature on the topic of fracture analysis of CNTRC for structural applications.

In this paper, a numerical XFEM-based framework is proposed to analyze crack-growth in CNT reinforced polymer composites that accounts for both the mechanical and piezoresistive behavior of the CNTRC. The objective is twofold: employing the numerical scheme to analyze how the crack affects the CNTRC mechanical integrity of the composite and further assess how its sensor performance is affected by cracking. To this end, the ANSYS software will be employed. The constitutive electro-mechanical modeling of the CNTRC composite follows a two-step procedure [17, 30]: (1) in a first step, the homogenization of the mechanical properties is conducted using a double-inclusion mean-field approach; (2) whilst the second step addresses the homogenization of the electrical conductivity and piezoresistivity properties, by implementing the model previously proposed by García-Macías et al. [36] and Buroni and García-Macías [37]. The parameters of this micromechanics model are adjusted in order to fit experimental results available in the literature [17]. Once the constitutive parameters are defined, the XFEM as implemented in ANSYS- is employed to solve the mechanical problem and compute the strain state in the cracked domain. Subsequently, strains are related to local changes in piezoresistivity, so that an additional non-homogeneous electrical conductivity problem has to be addressed. For this purpose, coupled-field elements are used. In this manner, we can correlate the crack-growth in the CNTRC with the electrical resistance change measured between electrodes. The proposed numerical framework is first validated for stationary cracks and later applied to several crack-growth configurations. The conducted numerical studies reveal that the presence of the crack and its growth significantly modify the electrical behavior and self-sensing capability of the CNTRC.

The remainder of the paper is organized as follows: Section 2 summarizes the micromechanics approach adopted to model both the mechanical and piezoresistive behavior of the CNT reinforced polymer. Section 3 presents and discusses the details of the computational XFEM-based framework implemented in ANSYS to analyze the electro-mechanical behavior of fractured CNTRC, both under stationary and crack-growth conditions. In Section 4, some numerical results are presented and discussed, in order to investigate the influence that the presence of a crack and its growth- has in the sensory performance of the CNTRC. Section 5 closes the paper by summarizing the most relevant conclusions of this study.

2. Micromechanics modeling of the electromechanical properties of MWCNT/epoxy nanocomposites

In the notation hereafter, blackboard-bold and bold letters are used to denote fourth-order ($\mathbb{A}$) and second-order tensors ($\mathbf{A}$), respectively. Colon notation is used to indicate the inner product between two fourth-order tensors $(\mathbb{A} : \mathbb{B})_{ijmn} \equiv A_{ijkl} B_{klmn}$.

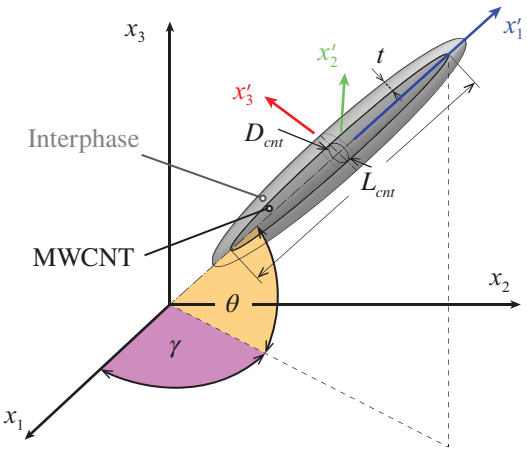

Figure 1: Euler angles defining the relation between the orientation of a MWCNT in the local coordinate system, K′ ≡ $\{0; x_1' x_2' x_3'\}$ and the global coordinate system, K≡ $\{0; x_1 x_2 x_3\}$.

2.1. Elastic properties

The elastic properties of MWCNT/epoxy nanocomposites are estimated in this work by adopting a core-shell interphase model [38, 39]. This approach embodies the filler/matrix interfacial properties through finite elastic coatings with constant thickness t surrounding the fillers (see Fig. 1). The composite is thus conceived as a three-phase composite, including the matrix, inclusions, and interphases with elastic tensors $\mathbb{C}_m$, $\mathbb{C}_p$ and $\mathbb{C}_i$, respectively. Following the double-inclusion method by Hori and Nemat-Nasser [40], the effective stiffness tensor of a Representative Volume Element (RVE) of a MWCNT/epoxy composite can be obtained as:

$$\overline{\mathbb{C}} = \left(f_m\mathbb{C}_m + f_i\langle\mathbb{C}_i : \mathbb{A}_i\rangle + f_p\left\langle\mathbb{C}_p : \mathbb{A}_p\right\rangle\right) : \left(f_m\mathbb{I} + f_i\langle\mathbb{A}_i\rangle + f_p\left\langle\mathbb{A}_p\right\rangle\right)^{-1}, \tag{1}$$

where f_p, f_i, and f_m denote the volume fractions occupied by fillers, interphases ratio, and the matrix phase, respectively. Angle brackets $\langle\cdot\rangle$ in Eq. (1) indicate orientational average in the space formed by Euler angles γ and θ shown in Fig. 1. Interfaces in MWCNT/epoxy composites are characterized by weak van der Waals (vdW) forces, which may be assimilated as penetrable soft interphases with volume fraction f_i [41, 42]:

$$\begin{aligned} f_i = (1-f_p)\Bigg(1 - \exp\Bigg\{-\frac{6f_p}{1-f_p}\Bigg[\frac{\eta}{n(s)} + \left(2 + \frac{3f_p}{n^2(s)(1-f_p)}\right)\eta^2 + \\ + \frac{4}{3}\left(1 + \frac{3f_p}{n(s)(1-f_p)}\right)\eta^3\Bigg]\Bigg\}\Bigg), \end{aligned} \tag{2}$$

where the term $\eta = t/D_{eq}$ denotes the ratio between the thickness t and the equivalent diameter D_{eq} of the interphases. The latter stands for the diameter of a sphere with volume equal to that of the particles. Given the aspect ratio of MWCNTs $s = L_{cnt}/D_{cnt}$, with L_{cnt} and D_{cnt} being the filler length and diameter, respectively, D_{eq} takes the form $D_{eq} = D_{cnt}s^{1/3}$ [41, 42]. The term $n(s)$ in Eq. (2) represents the sphericity of the fillers and is defined as:

$$n(s) = \frac{2s^{2/3}\tan\varphi}{\tan\varphi + s^2\varphi}, \tag{3}$$

where φ is given by $\varphi = \arccos(1/s)$. The concentration tensors in Eq. (1) for interphases and inclusions, $\mathbb{A}_i$ and $\mathbb{A}_p$, respectively, can be expressed in terms of the corresponding dilute concentration tensors, $\mathbb{A}_i^{dil}$ and $\mathbb{A}_p^{dil}$, as:

$$\mathbb{A}_\chi = \mathbb{A}_\chi^{dil} : \left(f_m\mathbb{I} + f_i\mathbb{A}_i^{dil} + f_p\mathbb{A}_p^{dil}\right)^{-1}, \quad \chi = p, i \tag{4}$$

$$\mathbb{A}_\chi^{dil} = \mathbb{I} + \mathbb{S} : \mathbb{T}_\chi, \quad \chi = p, i \tag{5}$$

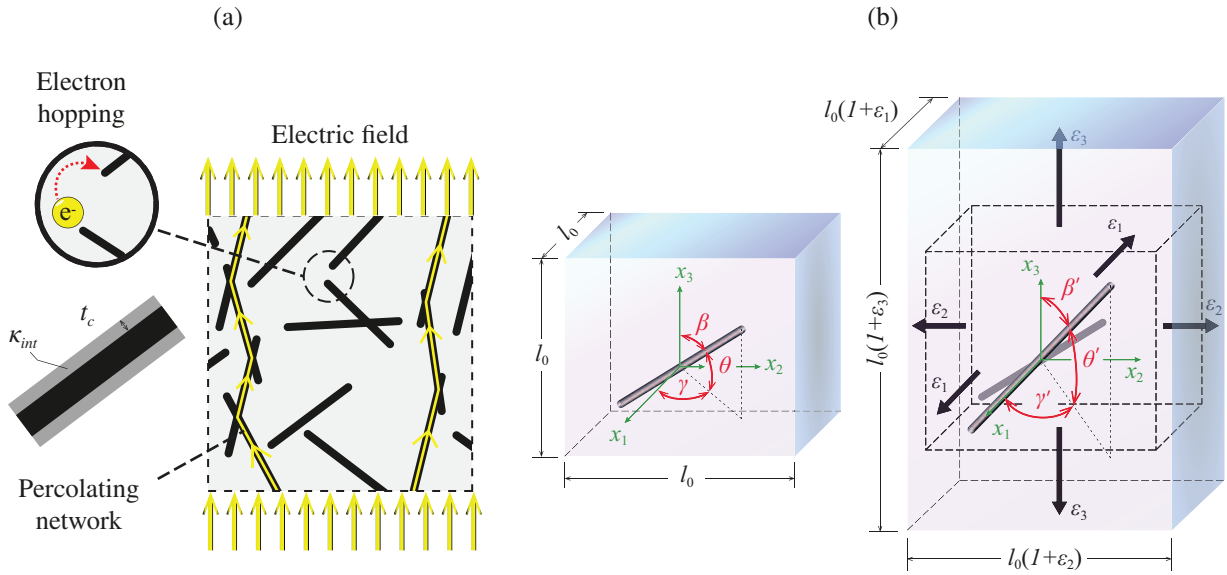

Figure 2: (a) Schematic of the conductive mechanisms governing the electrical conductivity of MWCNT/epoxy nanocomposites. (b) Deformable cubic cell containing an embedded filler under a tri-axial strain state ($\varepsilon_1, \varepsilon_2, \varepsilon_3$).

with

$$\mathbb{T}_\chi = -\left(\mathbb{S} + \mathbb{M}_\chi\right)^{-1}, \quad \chi = p, i \tag{6}$$

$$\mathbb{M}_\chi = \left(\mathbb{C}_\chi - \mathbb{C}_m\right)^{-1} : \mathbb{C}_m, \quad \chi = p, i \tag{7}$$

and $\mathbb{S}$ being the mechanical Eshelby's tensor for MWCNTs idealized as prolate ellipsoidal particles, and $\mathbb{I}$ the fourth-order identity tensor. Readers may refer to reference [43] for further details on the specific formulation of $\mathbb{S}$.

2.2. Electrical conductivity

Owing to the percolation-type behavior of CNT-based composites, their electrical conductivity experiences a sudden rise of several orders of magnitude when the filler concentration reaches the so-called percolation threshold, f_c. Below percolation ($f_p < f_c$), electrons can only travel between CNTs through a quantum tunneling effect, also known as electron hopping mechanism. However, once the percolation threshold is achieved ($f_p \geq f_c$), some fillers begin forming electrically conductive paths and both the electron hopping and the conductive networking mechanisms contribute to the composite's conductivity [44, 45] as sketched in Fig. 2 (a). The electron hopping mechanism can be modeled in the shape of interphases with electrical resistivity given by the generalized Simmons' formula [46]:

$$R_{int}(d_a) = \frac{d_a \hbar^2}{a e^2 \left(2m\lambda\right)^{1/2}} \exp\left(\frac{4\pi d_a}{\hbar}\left(2m\lambda\right)^{1/2}\right), \tag{8}$$

with m and e being the mass and the electric charge of the electron, respectively, λ the height of the tunneling potential barrier, a the contact area of the fillers, $\hbar$ the reduced Planck's constant, and d_a the average inter-particle distance. The latter is usually approximated in a piecewise form [44] as $d_a = d_c$ for $f_p < f_c$, and $d_a = d_c \left(f_c / f_p\right)^{1/3}$ for $f_p \geq f_c$, with d_c being the maximum filler separation at which tunneling penetration of electrons is possible. The thickness t_c and conductivity κ_{int} of the conductive interphases, as well as the volume fraction f_{eff} of the effective fillers (MWCNTs plus interphases) can be computed as [44, 47]:

$$t_c = \frac{1}{2} d_a, \quad \kappa_{int} = \frac{d_a}{a R_{int}(d_a)}, \quad f_{eff} = \frac{\left(D_{cnt} + 2t_c\right)^2 \left(L_{cnt} + 2t_c\right)}{D_{cnt}^2 \, L_{cnt}} f_p. \tag{9}$$

On this basis, MWCNT/interphase ensembles can be modeled as equivalent rod-like particles with transversely isotropic conductivity (refer to [44, 48] for further details), and the overall electrical conductivity of the composite can be estimated by the Mori-Tanaka method as [45, 49]:

$$\boldsymbol{\kappa}_{eff} = \boldsymbol{\kappa}_m + (1 - \xi_p) \langle \boldsymbol{\Gamma}_{EH} \rangle + \xi_p \langle \boldsymbol{\Gamma}_{CN} \rangle , \tag{10}$$

with

$$\boldsymbol{\Gamma}_{EH} = f_{eff} (\boldsymbol{\kappa}_{EH} - \boldsymbol{\kappa}_m) \mathbf{A}_{EH}, \tag{11}$$

$$\boldsymbol{\Gamma}_{CN} = f_{eff} (\boldsymbol{\kappa}_{CN} - \boldsymbol{\kappa}_m) \mathbf{A}_{CN}, \tag{12}$$

where subscripts EH and CN refer to the electron hopping and conductive networking mechanisms, respectively, and $\boldsymbol{\kappa}_m$ is the conductivity tensor of the matrix phase. The term ξ_p in Eq. (10) denotes the fraction of percolated MWCNTs, which can be approximated as [50]:

$$\xi_p = \begin{cases} 0, & 0 \leq f_p < f_c \\ \dfrac{f_p^{1/3} - f_c^{1/3}}{1 - f_c^{1/3}}, & f_c \leq f_p \leq 1 \end{cases} \tag{13}$$

Quantities related to the electron hopping and the conductive network mechanisms in Eqs. (10)-(12) are computed considering filler aspect ratios $s = L_{cnt}/D_{cnt}$ and $s = L_{cnt}/D_{cnt} \rightarrow \infty$ [47], respectively. In particular, the electric field concentration tensors $\mathbf{A}_{EH}$ and $\mathbf{A}_{CN}$ in Eqs. (11) and (12), respectively, can be obtained from the general form of the concentration tensor $\mathbf{A}$ [44]:

$$\mathbf{A} = \mathbf{A}^{dil} \left\{ \left(1 - f_{eff}\right) \mathbf{I} + f_{eff} \left\langle \mathbf{A}^{dil} \right\rangle \right\}^{-1} , \tag{14}$$

with $\mathbf{A}^{dil}$ denoting the dilute concentration tensor given by:

$$\mathbf{A}^{dil} = \left\{ \mathbf{I} + \mathbf{S} (\boldsymbol{\kappa}_m)^{-1} (\boldsymbol{\kappa}_c - \boldsymbol{\kappa}_m) \right\}^{-1} , \tag{15}$$

with $\mathbf{I}$ being the identity matrix. Assuming ellipsoidal inclusions with symmetry axis x_3, the components of the Eshelby's tensor $\mathbf{S}$ in Eq. (15) read ($s > 1$) [51]:

$$\begin{aligned} S_{22} &= S_{33} = \frac{s}{2\left(s^2-1\right)^{3/2}} \left[s \left(s^2 - 1\right)^{1/2} - \cosh^{-1} s \right], \\ S_{11} &= 1 - 2S_{22}. \end{aligned} \tag{16}$$

2.3. Piezoresistance modeling

Within the framework of the previously overviewed micromechanics approach, it is possible to estimate the piezoresistivity properties of MWCNT/epoxy composites through the incorporation of strain-induced alterations of the electron hopping and conductive networking mechanisms. Specifically, three main effects are commonly recognized in the literature [36, 52]: (i) volume expansion and reorientation of fillers, (ii) breakage of conductive paths, and (iii) variation of the inter-particle properties. The volume expansion and filler reorientation mechanisms can be simulated by the deformable cell model illustrated in Fig. 2 (b). As shown by the authors in reference [36], dilation-induced effects are usually more influential than those due to distortion. In this case, when an l_0-sided cubic cell loaded with a MWCNT is subjected to an arbitrary dilation strain $(\varepsilon_1, \varepsilon_2, \varepsilon_3)$, its volume changes from $V_0 = l_0^3$ to $V = l_0^3 \overline{\varepsilon}_1 \overline{\varepsilon}_2 \overline{\varepsilon}_3$, with $\overline{\varepsilon}_i = 1 + \varepsilon_i$ (see Fig. 2 (b)). The deformation is primarily sustained by the matrix, which is considerably more flexible than the MWCNT, thereby the apparent filler content varies as:

$$f^* = \frac{V_0 f}{V} = \frac{f}{\overline{\varepsilon}_1 \overline{\varepsilon}_2 \overline{\varepsilon}_3}. \tag{17}$$

Additionally, the embedded MWCNT also experiences a reorientation as an result of the applied dilation, which can be defined as a variation of the Euler angles from (γ,β) to (γ',β'). The closed-form expression of the strain-dependent orientation distribution function (ODF) under general dilation strains, $\Omega(\gamma',\beta')$, was derived by the authors as [36]:

$$\Omega(\gamma',\beta') = \frac{\bar{\varepsilon}_1^{-2}\bar{\varepsilon}_2^{-2}\bar{\varepsilon}_3^{-2}}{\left[\bar{\varepsilon}_2^{-2}\bar{\varepsilon}_3^{-2}\cos^2\beta' + \bar{\varepsilon}_1^{-2}\left(\bar{\varepsilon}_2^{-2}\cos^2\gamma' + \bar{\varepsilon}_3^{-2}\sin^2\gamma'\right)\sin^2\beta'\right]^{3/2}}. \tag{18}$$

No volume expansion is experienced by the composite when subjected to distortion, thereby the effective filler volume fraction remains unaltered and only filler reorientation takes place. Such reorientation effects can be estimated using a deformable cell model similar to the one previously shown in Fig. 2 (b). In the particular case of shear strain ε_{32} in the cell x_2-x_3 plane, the authors reported in reference [36] the corresponding closed-form expression for the distortion-dependent ODF as:

$$p(\gamma,\beta') = \left(1 - 4\varepsilon_{32}\sin\gamma\sin\beta'\cos\beta' + 4\varepsilon_{32}^2\sin\gamma\sin\beta'\right)^{-3/2}. \tag{19}$$

The filler reorientation induced by external mechanical strains reduces the randomness of the filler dispersion and, as a consequence, the percolation threshold increases. This effect can be accounted for by computing the percolation threshold f_c by means of the stochastic percolation model of Komori and Makishima [53], exploiting the strain-dependent ODFs reported in Eqs. (18) and (19) (refer to [36] for further details). Finally, mechanical strains may also affect the electron hopping mechanism through variations of the inter-particle distance d_a and the height of the potential barrier λ. Some research works in the literature suggest that, at low strain levels ($< 10^{-4}$), these magnitudes vary linearly with strain as [54]:

$$\begin{aligned} d_a &= d_{a,0}(1 + C_1\varepsilon), \\ \lambda &= \lambda_0(1 + C_2\varepsilon), \end{aligned} \tag{20}$$

where subscript 0 relates the corresponding quantities to the unstrained system. The terms C_1 and C_2 are proportionality constants, usually obtained by fitting experimental data.

In light of the formulation above, the relative change in resistivity of the plane-stress solids investigated hereafter can be related to the mechanical strain tensor $\boldsymbol{\varepsilon}$ as [36]:

$$\begin{bmatrix} \Delta\rho_{11}/\rho_0 \\ \Delta\rho_{22}/\rho_0 \\ \Delta\rho_{12}/\rho_0 \end{bmatrix} = \begin{bmatrix} \lambda_{11} & \lambda_{12} & 0 \\ \lambda_{12} & \lambda_{11} & 0 \\ 0 & 0 & \lambda_{44} \end{bmatrix} \begin{bmatrix} \varepsilon_{11} \\ \varepsilon_{22} \\ \varepsilon_{12} \end{bmatrix}, \tag{21}$$

where ρ_{ij} are the components of the resistivity tensor $\boldsymbol{\rho}_{eff} = \boldsymbol{\kappa}_{eff}^{-1}$, and ρ_0 is the resistivity of the composite in the absence of mechanical strains. The terms λ_{ij} denote the piezoresistivity coefficients. Specifically, λ_{11} represents the longitudinal piezoresistive effect, λ_{12} relates the transverse piezoresistive effect, and λ_{44} describes the shear piezoresistive effect. Once the strain sensitivity curves are obtained ($\Delta\rho_{ij}/\rho_0$), the piezoresistivity coefficients can be estimated as the slope of a linear regression (interested readers may refer to García-Macías et al. [36] for further theoretical details). Alternatively, the piezoresistivity coefficients λ_{ij} can also be obtained in closed-form by applying the formulation for the modeling of piezoresistive fiber-reinforced composites with percolation-type behavior proposed by Buroni and García-Macías [37] (further theoretical details can be found in [37], where open-source computer codes in MATLAB and Python languages with the corresponding implementation for the piezoresistive coefficient of CNT/epoxi composites are also presented).

3. Virtual crack growth monitoring of cracked nanocomposite panels

3.1. Mechanical problem solution

Consider a homogeneous and isotropic two-dimensional domain containing pre-existing cracks under complex loading state. Two kind of problems are considered: *stationary crack problems* and *crack-growth problems*. Upon growing, a planar crack under the mixed mode possibly kinks at a certain angle from its original plane. This angle

depends on the mixticity degree, or in other words, on the relative amount of mode II to mode I loading. Then, we can say that two criteria are required in order to decide if: (i) a pre-existing crack will grow, and if it does, (ii) in which direction. In order to model this complex mechanical problem appropriate computational methodologies are required. As mentioned at the introduction, XFEM technique is selected in this work. In this subsection we briefly review the key points for the analysis of mixed-mode cracking problems by means of XFEM methodology implemented in ANSYS Mechanical APDL 19.2 [22].

3.1.1. Direction of the kink

A propagating crack seeks the path of maximum driving force, so under mixed-mode it needs not to be confined to its initial plane. In the framework of a cohesive crack model, a crack-growth criterion must be specified for newly cracked cohesive segments to initiate ahead of the existing cracks [22]. In the literature, there exists several methods in order to decide which direction the kink crack takes, based both on energy or on stresses. However in ANSYS Mechanical APDL 19.2 implementation [22] only two criteria are available: maximum circumferential stress criterion and circumferential stress criterion based on $\sigma_{r\theta} = 0$. In this work the criterion by Erdogan and Sih [55] is selected, who by looking to experimental data propose that the kink angles are well predicted by the plane with the *maximum circumferential stress* when sweeping around the crack tip. Up to discretization issues, both methods yield the same result.

3.1.2. Crack growth criterion

For a *growing crack*, the XFEM formulation, as implemented in the commercial finite element package ANSYS Mechanical APDL 19.2 [22] does not account for the presence of singularities at the end of the cracks, then classical criteria based on Stress Intensity Factors are not available. Consequently, once the crack path is decided with above criterion, a mode I cohesive growth is herein considered. When the crack-growth criterion is reached ahead of the crack, new cohesive segments are introduced in the elements ahead of the current crack front, and crack propagation evolves. The new crack segments are such that they fully cut the elements ahead of the crack. The crack propagates at the rate of only one element at a time.

Fracture cohesive processes initiate at a given critical value of the normal stresses, σ_{max} (see Figure 3). As the normal displacement between the two surfaces of the cracked segment increases, the cohesive stresses in the cracked segment gradually decrease to zero as the deformation progresses. The decay of the cohesive stresses is modeled based on a rigid linear cohesive law [56]. Figure 3 shows the linear evolution evolution of the stresses in the newly cracked segments. The value of σ_{max} is taken from the fracture energy expression:

$$G_C = \frac{1}{2}\sigma_{max}\delta_n, \tag{22}$$

where G_C is the fracture energy and δ_n is the normal displacement jump at the completion of debonding. A detailed explanation about the values of the parameters considered in the cohesive law and the Eq.(22) will be presented in the following section.

3.1.3. XFEM formulation

It is well known that the XFEM provides a mesh independent approximation for the non-smooth mechanical problems with discontinuous and singular solutions, therefore it has been widely used in fracture mechanics simulations since the pioneering works of Belytschko et al. [19–21], Möes and Belytschko [57], Sukumar et al. [58] or Fries and Belytschko [59].

For *stationary crack analysis*, XFEM makes use of local enrichment functions to model the displacement field near the crack face (discontinuous field) and crack tip (asymptotic field). For instance, in two-dimensional crack modeling, the approximate displacement field for a four-nodes element can be expressed as [19, 20]:

$$\mathbf{u}(X) = \sum_{i=1}^{4} N_i(X) \left\{ \mathbf{u}_i + H(X)\, \mathbf{a}_i + \sum_{j=1}^{4} F_j(X)\, \mathbf{b}_i^j \right\}, \tag{23}$$

where $\mathbf{u}_i$ represents the nodal displacements vector, $N_i(X)$ denotes the conventional nodal shape functions, $H(X)$ stands for the Heaviside step function which takes values -1 or $+1$ depending on which side of the crack the sampling point

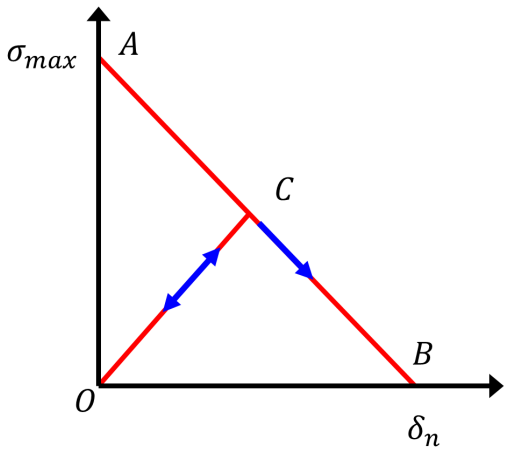

Figure 3: Linear evolution of the stresses in the newly cracked segments: the cohesive stresses in the cracked segment from A to B whereas the unloading and reloading path at any point C follows the path C-O.

is located, $\mathbf{a}_i$ is the enriched nodal degrees of freedom vector accounting for the jump in displacements, $F_j(X)$ are the crack-tip enrichment functions and $\mathbf{b}_i^j$ is the nodal degrees of freedom vector accounting for the crack-tip singularity (see Fig.4 (a)). The asymptotic crack-tip enrichment functions $F_j(X)$ are derived from the analytical solution of stress and displacement fields near the crack tip area. See for instance references [19, 58] for their expressions in isotropic materials:

$$\{ F_j(r,\theta) \}_{j=1}^4 = \left\{ \sqrt{r}sin(\theta/2) \; ; \; \sqrt{r}cos(\theta/2) \; ; \; \sqrt{r}sin(\theta/2)sin(\theta) \; ; \; \sqrt{r}cos(\theta/2)sin(\theta) \right\}, \tag{24}$$

with (r,θ) being the coordinates of a polar coordinate system with the origin centered at the crack tip. The interested reader is referred to reference [60] for the expressions of F_j in anisotropic elastic materials, or references [61] and [62] for piezoelectric and magnetoelectroelastic materials, respectively . The use of these special elements allows us to handle the crack tip asymptotic stresses in a straightforward manner, eliminating the need to remesh crack-tip regions when further conducting crack-growth simulations.

In this paper, the XFEM formulation, as implemented in the commercial finite element package ANSYS [22], is employed. To this end, ANSYS considers the following two methods:

- (i) Singularity-Based Method (SBM): the displacement functions in the FEM formulation are enhanced by introducing both the additional enrichment functions that capture the displacement jumps across the crack surfaces and the crack-tip singularities. SBM corresponds to the formulation sketched in Eq. (23). This will be the approach employed for the stationary crack analysis next presented. For this purpose, the four-nodes ANSYS element *PLANE-182* is considered under plane stress element behaviour.

- (ii) Phantom-Node Method (PNM) [63–66]: this method accounts only for the displacement jumps across the crack faces, while ignoring the crack-tip singularity contribution. This will be the approach employed in this paper to analyze static crack-growth problems. In the PNM, the crack-tip has to be located at the edge of a finite element and the displacement approximation for a four-nodes *PLANE-182* element becomes

$$\mathbf{u}(X) = \sum_{i=1}^{4} N_i(X) \{ \mathbf{u}_i + H(X) \, \mathbf{a}_i \}. \tag{25}$$

  However, introducing phantom nodes superposed on the parent element nodes as shown in Fig.4 (b), the displacement function can be rewritten in terms of the displacements of the real nodes and the phantom nodes [63] as a superposed element that splits the parent element into two subelements

$$\mathbf{u}(X,\tau) = \sum_{i=1}^{4} N_i(X) \left\{ H(-f(X)) \, \mathbf{u}_i^1(\tau) + H(f(X)) \, \mathbf{u}_i^2(\tau) \right\}. \tag{26}$$

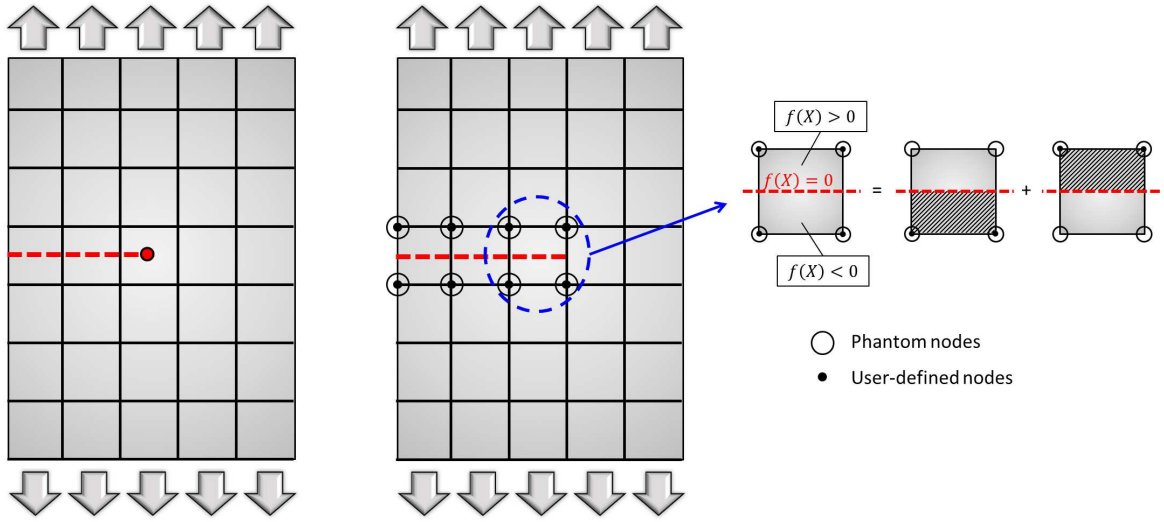

Figure 4: (a) Crack terminating inside the element. (b) Crack terminating at the edge of the element.

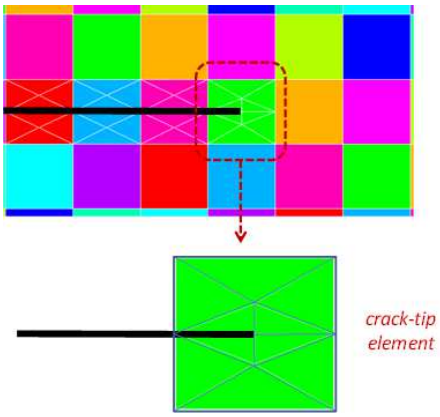

Figure 5: Partition of elements cut by the crack into sub-triangles for numerical integration in ANSYS.

In the expression above, τ represents the pseudo-time step, $\mathbf{u}_i^1$ and $\mathbf{u}_i^2$ are the nodal displacements vectors in subelement 1 and 2, respectively, $f(X)$ is the crack surface definition ($f(X) = 0$: Fig.4 (b) shows how the active part of element 1 holds for $f(X) < 0$ and consequently, the active part of element 2 holds for $f(X) > 0$) and $H(x)$ is the Heaviside step function

$$H(x) = \begin{cases} 1, & x > 0, \\ 0, & x \leq 0. \end{cases} \tag{27}$$

Regarding the numerical integration over the enriched elements, ANSYS overcomes the discontinuity along the crack by partitioning the affected elements into sub-triangles, as Fig.5 depicts (see for instance refs. [19, 20] for details on how to deal with the numerical integration of the X-FEM enriched functions and overcome the difficulties associated to both the discontinuity along the crack and the singularity at the crack tip).

3.1.4. Fracture energy

The addition of the MWCNTs into the epoxy results in a nanocomposite which exhibits enhanced strength and stiffness and, even more important, a significant increase in fracture toughness. These behaviours are for instance reported in Gojny et al. in [6], where the fracture toughness of CNT-based polymeric nanocomposites was investigated.

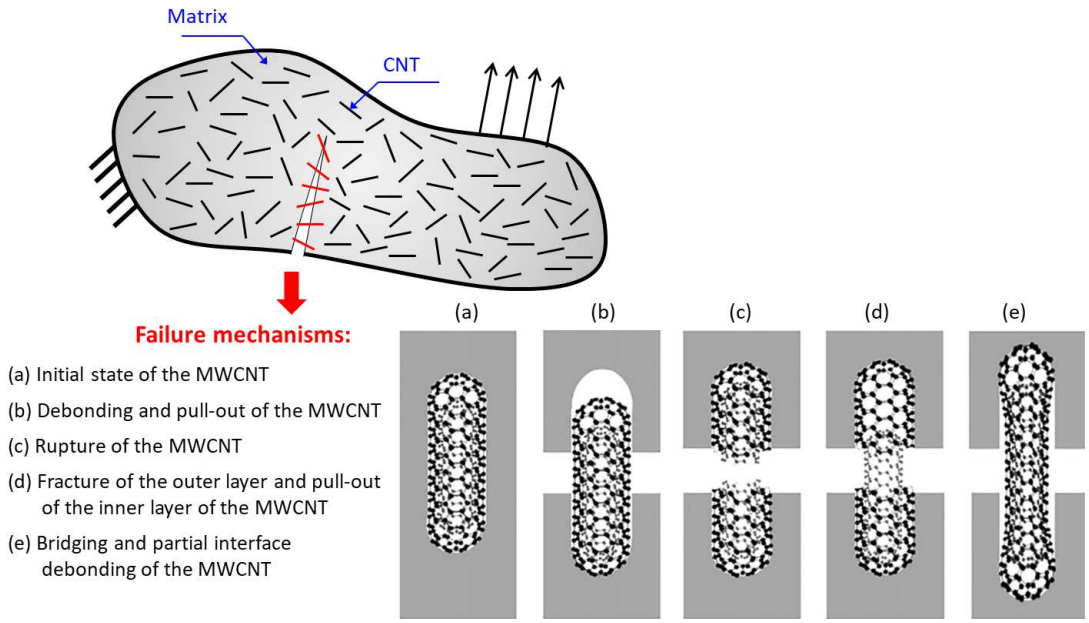

Figure 6: Schematic description of possible fracture mechanisms of CNTs [6]: (a) Initial state of the CNT; (b) pull-out caused by CNT/matrix debonding in case of weak interfacial adhesion; (c) rupture of CNT strong interfacial adhesion in combination with extensive and fast local deformation; (d) telescopic pull-out fracture of the outer layer due to strong interfacial bonding and pull-out of the inner tube; (e) bridging and partial debonding of the interface local bonding to the matrix enables crack bridging and interfacial failure in the non-bonded regions.

Table 1: Fracture energy experimental values [7].

MWCNT (*wt*%)	0	0.1	0.2	0.5
G_C (J/m^2)	133	162	188	223

They also showed that the highest value of fracture toughness was obtained when the CNTs were well dispersed in the polymer, as expected.

More recently, Hsieh et al. [7] showed that the fracture toughness (K_C) and fracture energy (G_C) of the epoxy polymers increased steadily as the nanotube content was increased. They measured how the value of G_C increased from 133 J/m^2 (for the unmodified epoxy) to 223 J/m^2 by the addition of 0.5 *wt*% of MWCNTs (see Table 1). Moreover, they observed in the fracture surfaces: river lines typical of brittle failures and the evidence which reveals the origin of the toughening mechanisms: nanotube pull-out and bridging can be clearly observed. Here, the mean pulled-out length is 7.8 μm, with a standard deviation of ±2.8 μm. Note that the MWCNTs are typically 120 μm long after sonication, so the measured average pulled-out length is much shorter than the nanotube length. Thus, the suggested sequence of events is that the nanotubes will first debond from the matrix to allow pull-out. However, as the nanotubes are long and not straight, they rupture rather than pulling-out completely. Therefore, energy will be absorbed by debonding, by friction between the nanotube and the polymer as it is pulled-out and by fracture of the nanotubes. These works [6, 7] also reported in their studies that the main observed toughening mechanisms were nanotube pull-out, plus debonding and plastic void growth (see Fig.6). The sword-in-sheath pull-out could also be considered as a toughening mechanisms. For the sword-in-sheath breaking mechanism, the outer shell of the MWCNT fractures in tension and the inner shells pull-out from within it. However, as no shell were observed in the voids, the sword-in-sheath pull-out mechanism can be discounted.

In this work, an addition of 0.5 *wt*% of MWCNTs is next considered for our analysis. Therefore, assuming G_C = 223 J/m^2 for the fracture energy value and δ_n = 7.5 μm for the normal displacement jump at the completion of debonding, the value of the maximum stress consistent with the Eq.(22) is: σ_{max} = 60 MPa.

Table 2: Effective electromechanical properties of the MWCNT/epoxy [17, 41].

wt%	E (GPa)	ν	κ (Sm^{-1})	λ_{11}	λ_{12}	λ_{44}
0.5	2.86	0.28	1.22×10^{-2}	6.84	7.99	1.19

3.2. Electrical problem solution

The electric resistance between two electrodes of the damaged nanocomposite domain can be computed and, by comparison with the electric resistance measured for the undamaged domain, we can detect the presence of a crack and its severity. For this reason, the electrostatic field in a non-homogenous domain needs to be computed, in absence of space-charge density, by solving the partial differential equation,

$$\nabla \cdot (\boldsymbol{\kappa} \nabla \phi) = 0. \tag{28}$$

This equation describes the electric potential (ϕ) distribution within a given region Ω_{el} characterized by a non-homogenous electric conductivity tensor $\boldsymbol{\kappa}$, which can be computed as $\boldsymbol{\kappa} = \boldsymbol{\rho}^{-1}$ where $\boldsymbol{\rho}$ denotes the electrical resistivity tensor.

Due to the piezoresistive behavior of the CNT-reinforced composite material, once the strains have been computed inside the domain and, therefore, the non-homogeneous electrical conductivity (or its inverse, the electrical resistivity) is known at each internal point, it is possible to solve the corresponding electric problem to characterize how the presence of the crack affects the electrical conductivity. According to Eq. (21), the relative resistivity changes ($\mathbf{r} = \Delta\boldsymbol{\rho}/\rho_o$) can be computed as: $\mathbf{r} = \boldsymbol{\Pi}\boldsymbol{\varepsilon}$. Consequently, the non-homogenous electric resistivity tensor can be computed as discussed above [17, 36], from:

$$\boldsymbol{\rho} = \rho_o(\mathbf{I} + \mathbf{r}) = \rho_o(\mathbf{I} + \boldsymbol{\Pi}\boldsymbol{\varepsilon}). \tag{29}$$

Adopting the electrodes configuration similar to the cracked plate presented in Fig. 7, one simple way to quantify the electric resistivity changes induced by the presence of a crack in the cracked plate would be to evaluate the electric resistance between electrodes (R) of the damaged plate and compare its value with the electric resistance measured for the undamaged plate (R_o). The electric resistance (R) of a plate of thickness t can be computed as

$$R = \frac{\Delta\phi}{I}, \tag{30}$$

where $\Delta\phi = \phi_1 - \phi_o$ is the voltage difference recorded between electrodes and I is the electric current flowing through the plate, which may be computed from the electric flux density $\mathbf{J}$ ($\mathbf{J} = -\boldsymbol{\kappa}\nabla\phi$) as

$$I = \int_A \mathbf{J}\mathbf{n} \mathrm{d}A \approx \int_{-l}^{+l} \mathbf{J}\mathbf{n} t \mathrm{d}x. \tag{31}$$

with t being the plate thickness.

It should be emphasized that, even though the mechanical problem is homogeneous, due to the piezoresitive behavior of the MWCNT reinforced composite (i.e. elastic deformations cause electrical conductivities variations) and to the electrical-conductivity discontinuities produced by the crack, the electrical problem (28-31) has to be solved under non-homogeneous electrical conductivities conditions. We follow such a two-step algorithm, based on first solving the mechanical XFEM fracture problem and , subsequently defining the corresponding electrical problem because the current *ANSYS* XFEM implementation does only support linear elastic isotropic material behaviour (i.e., it does not directly support coupled field elements).

The electrical problem is also solved by using the commercial finite element package *ANSYS*. In this case, the *ANSYS* element *PLANE-223* is considered. This element supports the piezoresistive physic, among others. The information about the elements which are located in the crack is transferred from an output file generated by the mechanical problem solution.

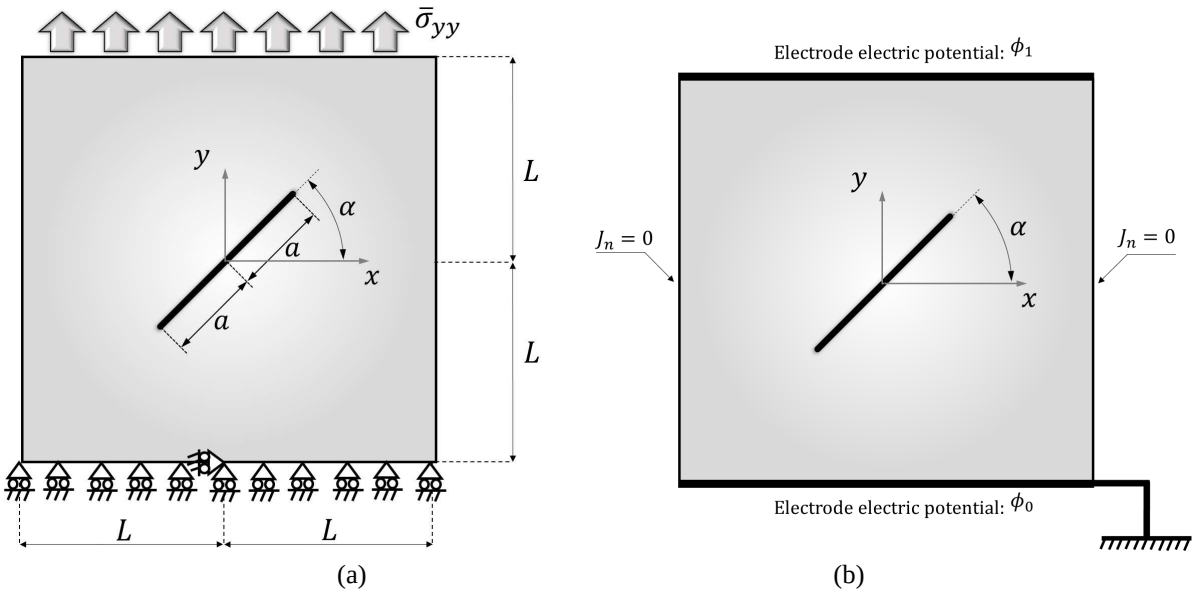

Figure 7: (a) Cracked plate under uniform stress ($\bar{\sigma}_{yy}$). (b) Electrodes position in the cracked MWCNT/epoxy composite plate.

3.3. Crack growth monitoring based on resistance changes

The following solution scheme is proposed in order to monitor the crack growth based on electrical resistance changes. The three main steps are summarized in Fig. 8 and consist in:

I. Solve the quasi static crack-growth analysis using the PNM. For every mechanical load step, the crack elements and the tip coordinates are stored in an output file which will be considered in the step II.

II. For every mechanical load step, we should solve an electrical (piezoresistive) problem considering the same element mesh and element numbering as the step I. As the crack elements numbers are known from the previous step, we can deactivate these elements to take into account the discontinuity in the electric field caused by the crack. In time step, the electric piezoresistive properties are updated from the mechanical strains computed in eachelement at step I. Subsequently, the electric potential can be computed and the electric flux density in the electrodes can be stored for every load step in another output file.

III. Finally, the electric resistance between the electrodes is computed for every load step according to (30) and (31). So the presence of the crack and its growth can be monitored via the electric resistance changes.

For the sake of completeness, a flowchart scheme has been included in Appendix A. It illustrates the solution scheme with ANSYS.

4. Crack detection: numerical studies

4.1. Stationary crack analysis

The proposed virtual monitoring scheme presented in this work (see Fig. 7) is applied to detect damage in a cracked MWCNT/epoxy composite plate due to several inclined crack configurations. In the following studies, the electromechanical properties considered for the MWCNT/epoxy composite were presented in Table 2 for 0.5 *wt*% of MWCNT. The theoretical predictions in this table have been obtained by inverse calibration of the micromechanics model previously presented in Section 2. To do so, the model parameters have been computed through gradient descent minimization of the mean squared errors between experimental data and the theoretical predictions as reported in a previous work by the authors in reference [41]. For completeness, the comparison between the theoretical predictions

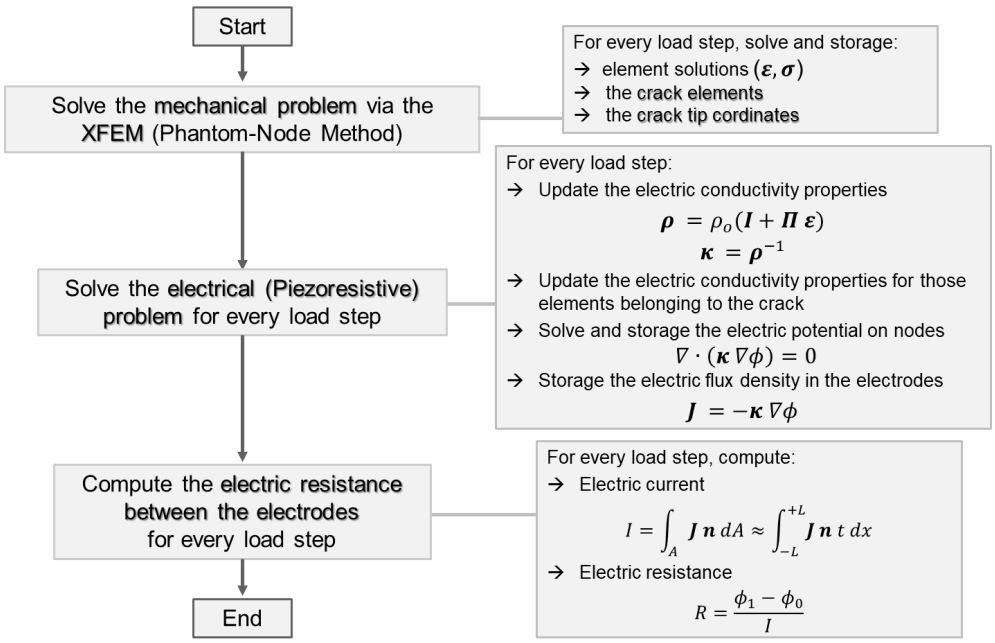

Figure 8: Solution scheme.

of the piezoresistive coefficients of MWCNT/epoxy composites using the micromechanics approach presented in Section 2.3 and the experimental characterization results reported by Sanli et al. [67] is reported in Appendix B.

Firstly, a stationary crack analysis using the XFEM under plane stress conditions is solved to show the accuracy of the finite element mesh adopted in Fig. 9 for $L/a = 10$ and a crack a crack angle $\alpha = 45^o$. Fig. 10 (a) shows the influence of the crack orientation angle (α) on the stress intensity factors K_I/K_o and K_{II}/K_o (being $K_o = \bar{\sigma}_{yy}\sqrt{\pi a}$), by comparison with the theoretical solution [68]. The XFEM results show an excellent agreement with the analytical solution. The resulting mesh has been selected after conducting the corresponding convergence studies. For instance, Fig. 10 (b) presents a convergence study on $K_I(\alpha = 60^o)$ and $K_{II}(\alpha = 60^o)$.

4.1.1. Resistance changes: influence of the crack size

After the above validation, we next analyze the influence of the crack size on the electric resistance changes in the damaged plate. So, the electrical problem has been solved with the same mesh, under both permeable and impermeable crack-face electrical boundary conditions, to study the influence of the crack size parameter (L/a) on the electric resistance. The prescribed electric potentials on the electrodes are: $\phi_o = 0$ V and $\phi_1 = 10$ V (see Fig. 7(b)). These results are presented in Fig. 11, taking into account several orientations (α) of the crack. Results were computed under both piezoresistive (dotted line) and non-piezoresistive (continuous line) conditions. The electrical piezoresistive problem has been solved using the *ANSYS* element *PLANE-223* and the electrical (non-piezoresistive) problem has been solved using the element *PLANE-121* [22].

We can see how the resistance (R) relative to the undamaged plate resistance (R_o) increases with the crack size (a), or in other words, with the decrease of the ratio L/a (see Fig. 11), as expected . Moreover, the resistance (R) also increases for decreasing values of angle α (the orientation of the crack relative to the electrodes). So, it is clear that the electric field is affected by the crack size and the crack orientation. Fig. 12 illustrates the electric potential distributions for $L/a = 5$ and two crack orientations: $\alpha = 0^o$ and $\alpha = 45^o$. However, the influence of the piezoresistive behaviour of the material on the electric resistance changes is not so significant, when compared with the changes caused by the presence of the damage, i.e., the crack. In Fig. 11, the dotted lines (piezoresistive analysis) are almost coincident with the continuous lines (non-piezoresistive analysis).

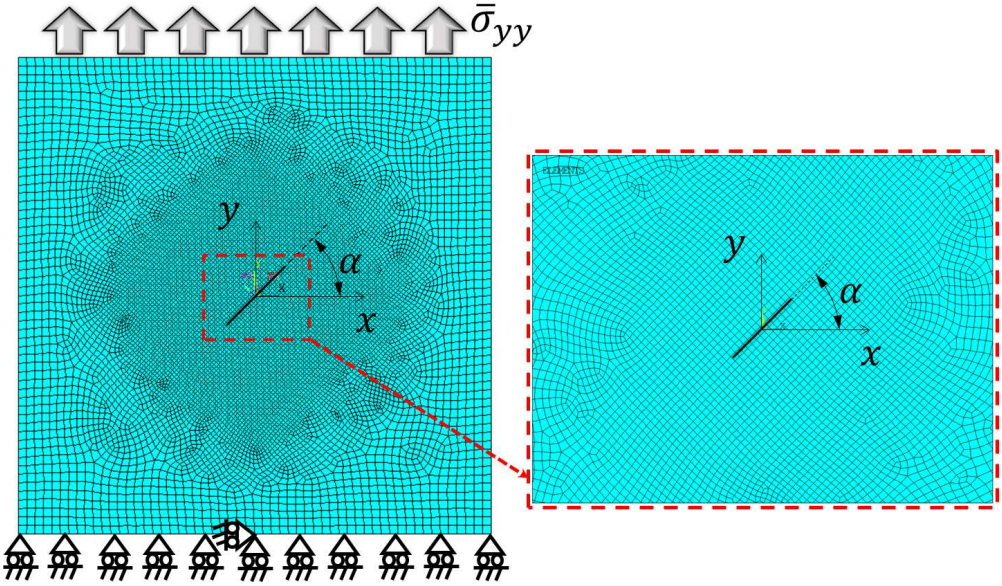

Figure 9: Mesh details for the stationary crack analysis using the XFEM.

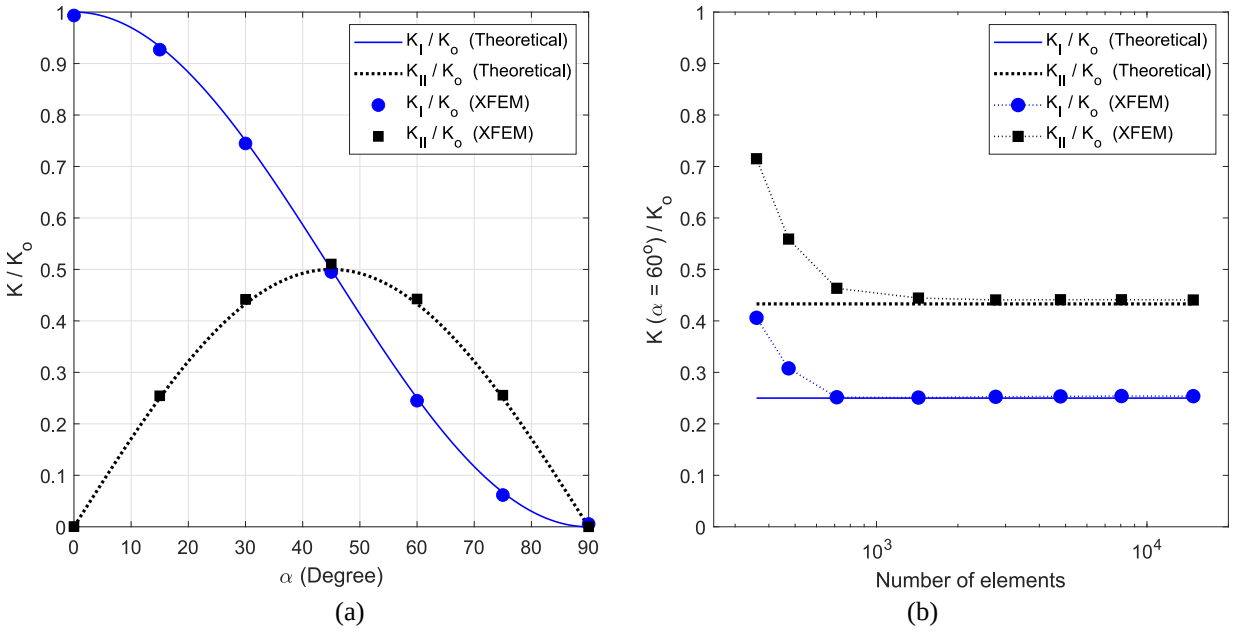

Figure 10: (a) Influence of the crack orientation (α) on the stress intensity factors: K_I/K_o and K_{II}/K_o, being $K_o = \bar{\sigma}_{yy}\sqrt{\pi a}$. (b) Convergence study on $K_I(\alpha = 60^o)$ and $K_{II}(\alpha = 60^o)$.

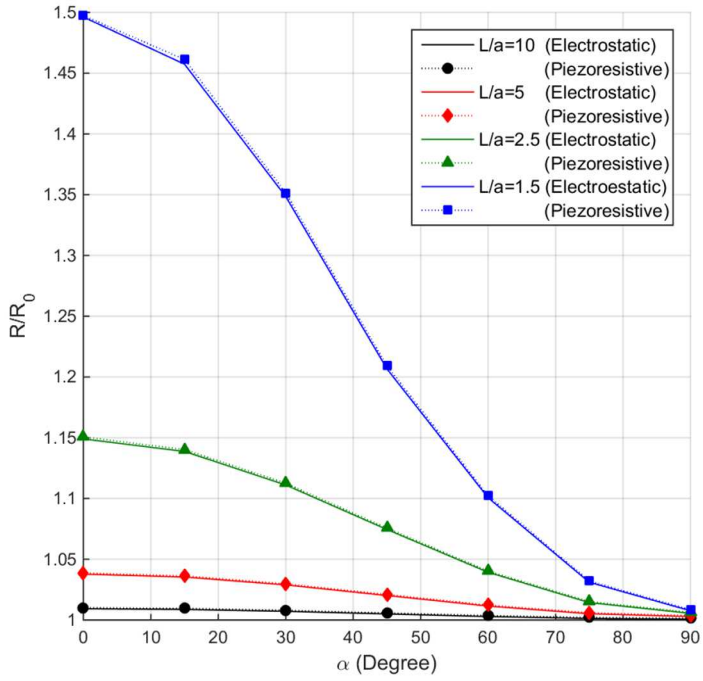

Figure 11: Influence of the size of the crack (L/a) and the crack orientation (α) on the electric resistance changes for both: electrostatic and piezoresistive models. In this figure, R_o is the electric resistance of the undamage plate.

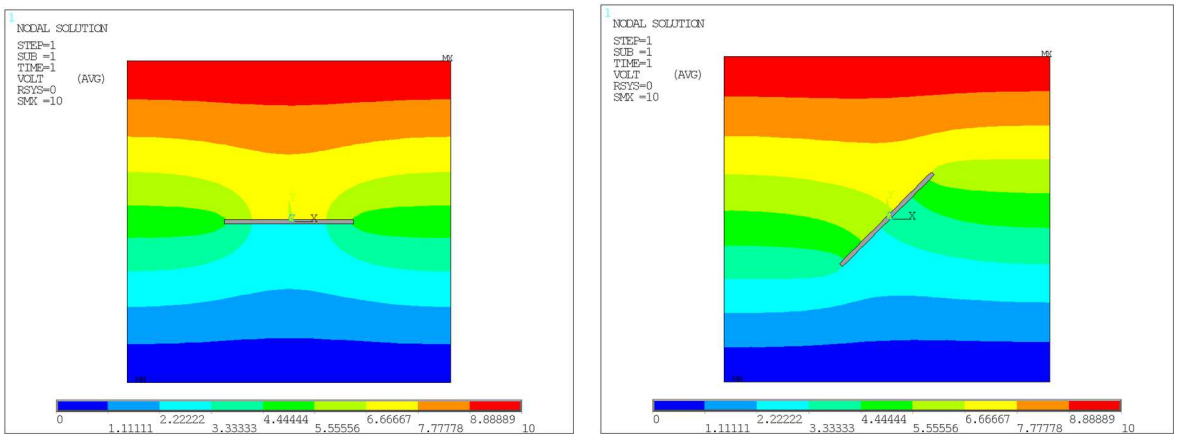

(a) (b)

Figure 12: Electric potential (ϕ) $[V]$ distribution for $L/a = 5$, $\phi_o = 0\ V$, $\phi_1 = 10\ V$ and the crack orientations: (a) $\alpha = 0^o$ and (b) $\alpha = 45^o$.

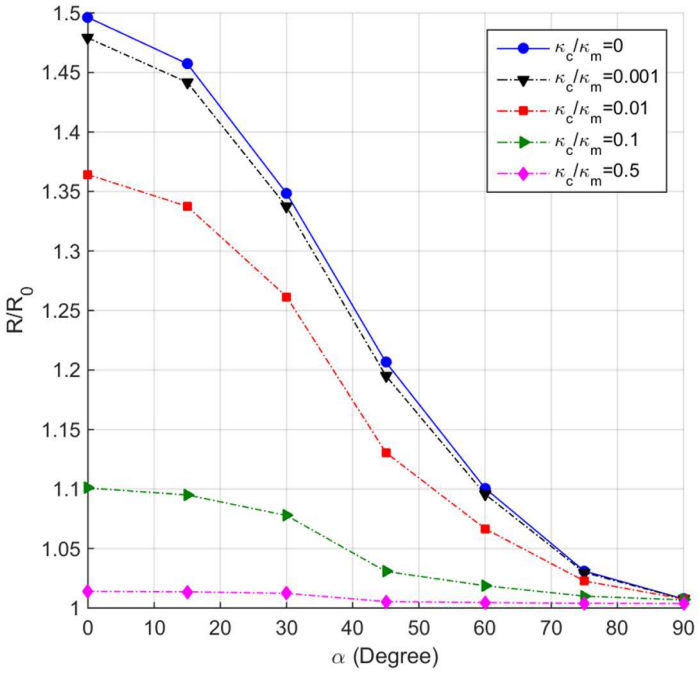

Figure 13: Influence of the crack permittivity conditions (κ_c/κ_m) and the crack orientation (α) on the electric resistance changes.

4.1.2. Resistance changes: influence of the electric permittivity crack conditions

It is also important to consider the crack-face electric permittivity conditions. Namely permeable, impermeable and semipermeable crack conditions are next considered. The crack permittivity is designated as κ_c and its values oscillate between $\kappa_c \approx 0$ (i.e., impermeable crack conditions) and $\kappa_c \approx \kappa_m$ (i.e., perfectly permeable crack conditions), being κ_m the electric conductivity of the undamaged and the unstrained plate.

For the damaged plate with $L/a = 3$, Fig. 13 shows the influence of the crack permittivity conditions (κ_c/κ_m) and the crack orientation (α) on the electric resistance ratio (R/R_o), being R_o the electric resistance of the undamaged plate. We can observe how the electric permeability of the crack is another parameter that determines the electric resistance of the plate. The more impermeable crack face conditions are, the greater is the electric resistance observed in the crack. This is easily observed in Fig. 14, where the electric potential distribution are presented for $L/a = 5$, $\alpha = 45^o$ and the crack permittivity conditions: (a) $\kappa_c/\kappa_m = 0.0001$ and (b) $\kappa_c/\kappa_m = 0.5$.

4.1.3. Resistance changes: two cracks configurations

To conclude the stationary crack analysis, we next analyze whether the present methodology could identify more than one defect, i.e., could distinguish between a single horizontal crack and two horizontal cracks. For this purpose, the two horizontal cracks configuration sketched in Fig. 15 is considered. Both cracks have the same semilenght (a_2) and their location is defined by δ_x, i.e., the horizontal distance between the crack tips, and δ_y, i.e., the vertical distance between them. In this case, impermeable crack-face electric permittivity conditions are considered: $\kappa_c = 0$ and the value of both cracks size parameter is: $L/a_2 = 5$. The same material properties as in the previous examples are adopted for the plate. Only electrical behaviour is considered in this example, while the piezoresistive behaviour of the material is not modeled in this case, once checked its low influence on the results for stationary crack configuration (as Section 4.1.1 illustrates)

Influence of the relative position between both cracks (i.e., δ_x and δ_y) on the electric resistance ($R_{2cracks}$) is studied. In order to see the difference between the electric resistance with one single cracked domain, the electric resistance ratio $R_{2\ cracks}/R_{1\ crack}$ is presented in Fig. 16, where R_{1crack} is the electric resistance computed for a single cracked domain whose crack semilength is $a_1 = 2a_2$.

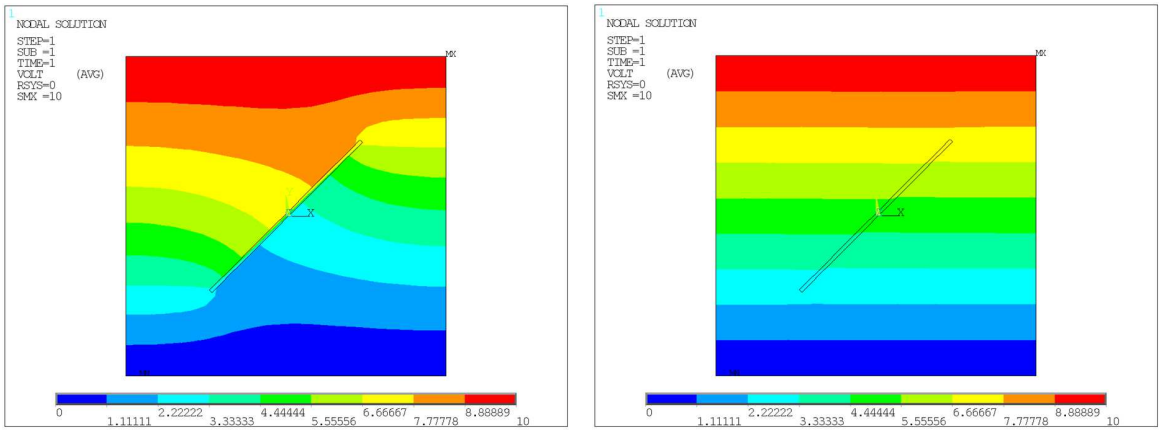

Figure 14: Electric potential (ϕ) [V] distribution for $L/a = 5$, $\phi_o = 0\ V$, $\phi_1 = 10\ V$ and $\alpha = 45^o$ crack permittivity conditions: (a) $\kappa_c/\kappa_m = 0.0001$ and (b) $\kappa_c/\kappa_m = 0.5$.

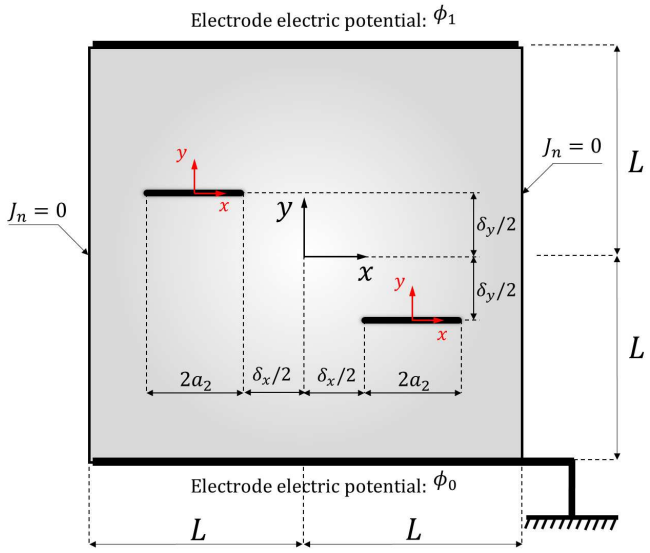

Figure 15: Location of two cracks in a MWCNT/epoxy composite plate.

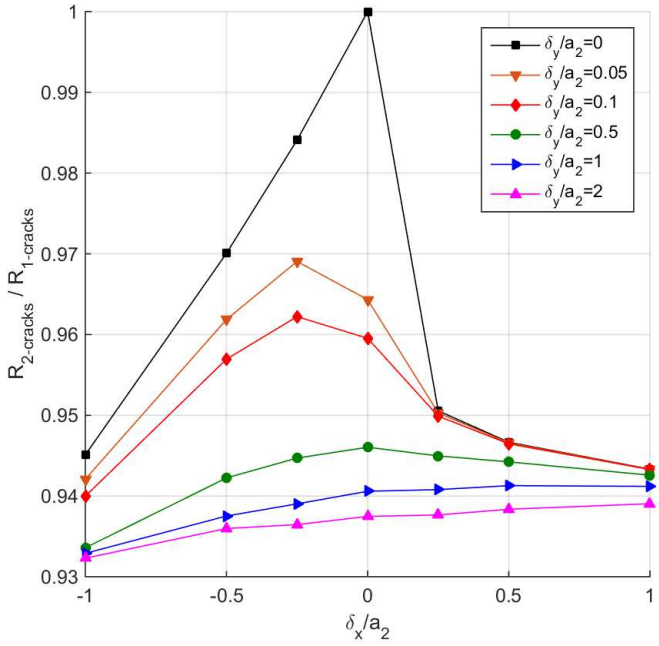

Figure 16: Influence of the relative positions (δ_x,δ_y) of the two cracks on the electric resistance.

We can observe in Fig. 16 how the electric resistance ratio ($R_{2\ cracks}/R_{1\ crack}$) is equal to one, when $\delta_x = 0$ and $\delta_y = 0$. However, important differences are observed when $|\delta_x| > 0$ and/or $|\delta_y| > 0$. For instance, let us observe the two cases showed in Fig. 17, where the electric potential (ϕ) distribution as a function of $\delta_y/a_2 = \{0, 0.5, 2\}$ is presented for $\delta_x = 0$ in Fig. 17 (a) and $\delta_x/a_2 = 0.5$ in Fig. 17 (b). When $\delta_x = 0$, the greater δ_y is, the lower is the electric resistance observed. The same behaviour is observed for $|\delta_x| > 0$. However, different resistances are observed between $|\delta_x| > 0$ and $|\delta_x| < 0$. This could allow us to correlate the crack configurations with the recorded electric resistance changes.

4.2. Crack-growth monitoring

This section presents two examples where the virtual crack-growth monitoring is developed. The first example considers a plate with an interior crack, under imposed vertical displacements. The second examples studies a three-point bending problem with an initial traction-free crack at the middle of the bottom edge of the specimen. Both analyses consider the same material, a MWCNT/epoxy composite with a 0.5% weight content of MWCNTs (see Table 2).

4.2.1. Cracked plate

The crack-growth analysis is applied on a MWCNT/epoxy composite square ($2L \times 2L$) plate with an interior inclined crack (see Fig. 18 (a)). The value of the plate length is $L = 0.1\ m$, the initial semilength of the crack is $a_o = 0.01$ m and two angles are considered: $\alpha = 0^o$ and $\alpha = 45^o$. The specimen is subjected to imposed vertical displacements ($\overline{u}_y$) on the upper edge of the domain. For the electrical problem, the electrodes position in the plate presents the same configuration as it was described in Fig. 7 (b), with $\phi_o = 0$ V and $\phi_1 = 10$.

The numerical simulations are performed under plane stress and electrical impermeable crack permittivity conditions, considering the very fine mesh presented in Fig. 18 (b). The election of the mesh has been done taking into account the convergence study presented on Fig.19, where the plate response diagrams are presented. Fig. 19(a) shows the resultant reaction force (F/F_o) on the lower face of the plate ($y = -L$) versus the vertical displacement on the upper face of the plate (i.e., u_y/u_o at $y = L$). 19(b) shows the crack extension (a/L) versus the vertical displacement u_y/u_o at $y = L$. The displacement is presented relative to the imposed vertical displacement,i.e., $u_o = \overline{u}_y$, and the reaction force (F) is presented divided by the theoretical reaction on the undamaged plate: $F_o = EAu_o/2L$.

$\delta_y/a_2 = 0$

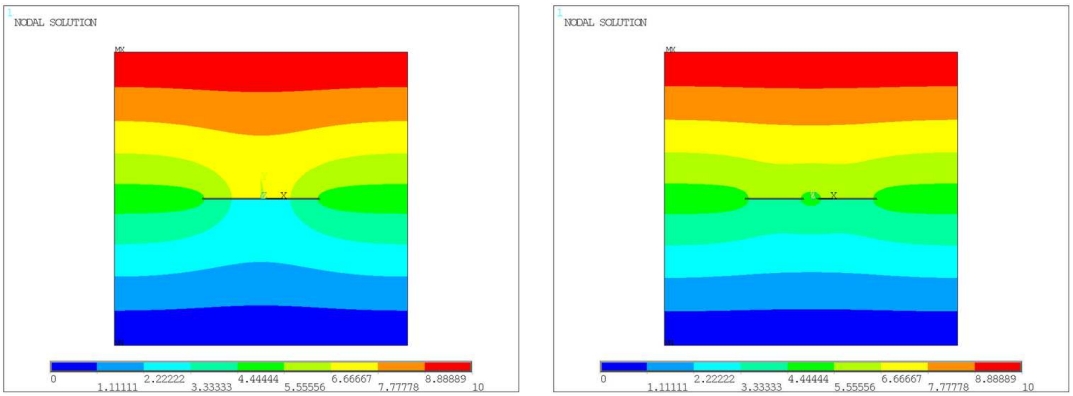

$\delta_y/a_2 = 0.5$

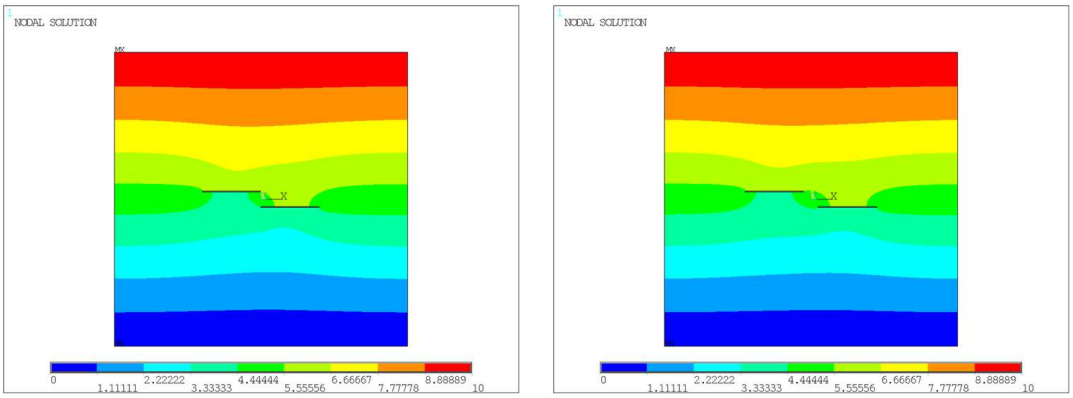

$\delta_y/a_2 = 2$

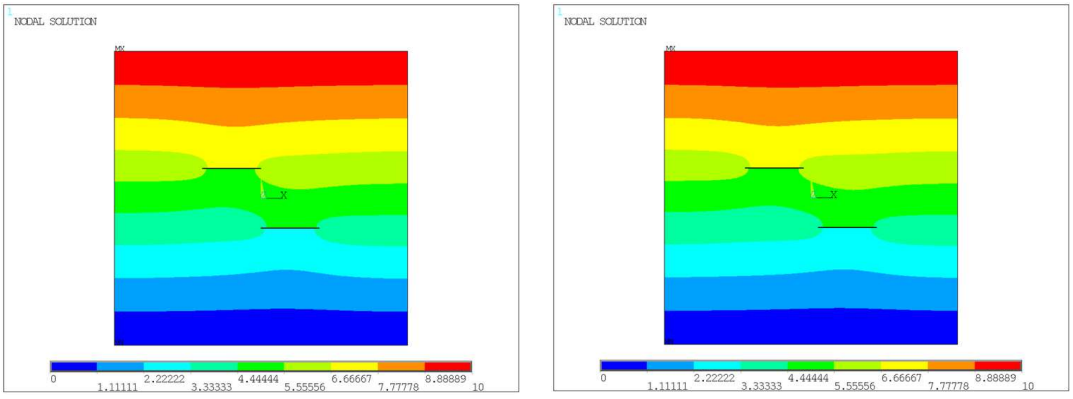

(a) (b)

Figure 17: Electric potential (ϕ) [V] distribution as a function of $\delta_y/a_2 = \{0, 0.5, 2\}$ for: (a) $\delta_x/a_2 = 0$ and (b) $\delta_x/a_2 = 0.5$.

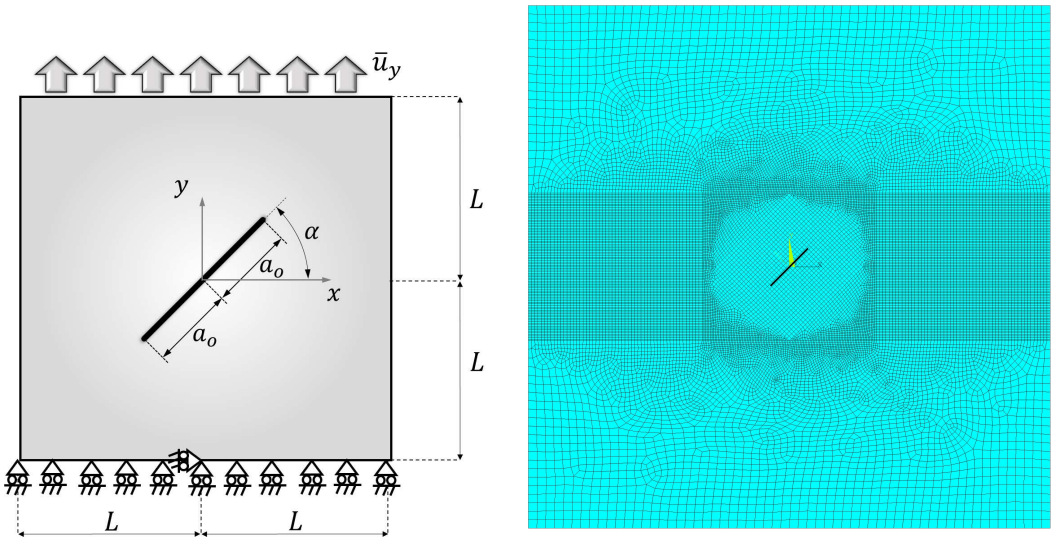

Figure 18: (a) Cracked plate under imposed vertical displacements ($\bar{u}_y$). (b) Mesh details for the crack-growth analysis using the XFEM.

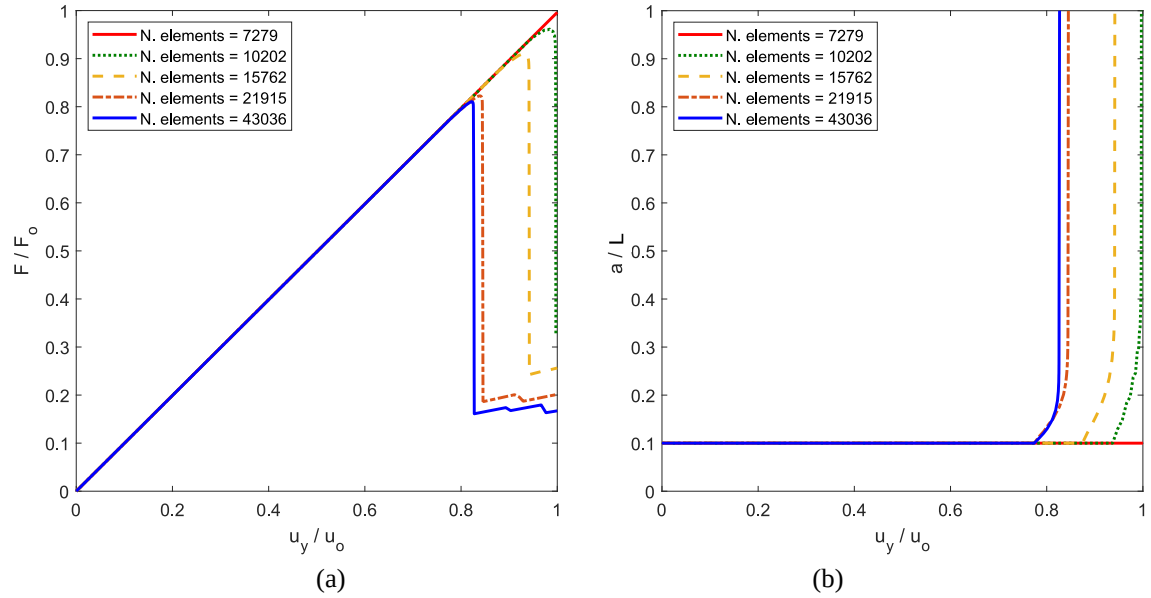

Figure 19: Convergence study on the plate response diagrams: (a) the resultant reaction force on the lower face of the plate (F/F_o) versus the vertical displacement on the upper face of the plate (i.e., u_y/u_o at $y = L$), (b) the crack extension (a/L) versus the vertical displacement u_y/u_o at $y = L$.

The coordinate of the crack tip and the electric potential distributions are computed for every load step. The evolution of the vertical displacements (u_y) and the electric potential (ϕ) distributions are presented in Fig. 20 (a) and Fig. 20 (b), respectively, caused by an inclined ($\alpha = 45^o$) crack growth.

Additionally, the electrical resistance between the electrodes is computed, according to Eq. (30) and Eq. (31), for every load step. Consequently, the crack tip coordinates and the electric resistance are known for every load step. Therefore, the electric resistance changes caused by the crack growth can be analyzed. Fig. 21 presents the electric resistance changes caused by a horizontal crack growth (blue lines) and an inclined crack growth (black lines). The evolution of the electric resistance (R) with the crack length (a) is showed in Fig. 24, where the electric resistance is presented relative to the electric resistance of the undamaged plate (R_o), i.e., when $a_o = 0$. The crack length is presented relative to the initial crack length (a_o). Results have been computed under piezoresistive (dotted line) and non-piezoresistive (continuous line) conditions. We can observe the same behaviour as the one observed in Section 4.1 for the stationary crack case, i.e., the influence of the piezoresistive behaviour on the electric resistance changes is not so significant when compared with the changes induced into the electric field by the presence of the crack.

4.2.2. Three-point flexural test

This last numerical example solves the three-point bending problem with an initial traction-free crack at the middle of the bottom edge of the MWCNT/epoxy composite specimen presented in Fig. 22 (a). The length of the beam is $L = 0.1$ m, the height of the beam is $W = 0.03$ m and the initial crack length in $a_o = 0.005$ m. This beam is subjected to a prescribed displacement ($\overline{u}_y$) boundary condition which is applied at the center of the top edge of the beam. Regarding the electrical boundary conditions on the specimen, Fig. 22 (b) shows the electrical boundary conditions, being the electrodes located at both ends of the beam. Moreover, impermeable crack permittivity conditions are considered not only in the initial crack, but also during the crack growth.

The very fine mesh presented in Fig. 22 (c) has been considered to solve both, the crack growth mechanical problem and the electrical problem, according to Section 3. Similarly to previous numerical studies, the electrical problem is solved including the piezoresistive behaviour (*PLANE-223 ANSYS* element) and the electrical (non-piezoresistive) behaviour (*PLANE*-121 *ANSYS* element). Fig. 23 presents the convergence study developed on the beam response diagrams to select the proper mesh for the studies. Fig. 23(a) shows the load deflection-curve, i.e., vertical reaction force (F/F_o) versus the vertical displacement (u_y/u_o) at $x = L/2$ and Fig. 23(b) presents the crack extension (a/W) versus the maximum deflection of the beam (i.e., u_y/u_o at $x = L/2$). The deflection is presented relative to the imposed vertical displacement,i.e., $u_o = \overline{u}_y$, and the reaction force (F) is presented divided by $F_o = 48EI_o u_o/L^3$, where I_o is the damage cross-section moment of inertia: $I_o = (W - a_o)^3/12$. The convergence analysis reveals the importance of selecting a fine mesh for the studies.

The evolution of the electric resistance (R) with the crack length (a) is showed in Fig. 24, where the electric resistance is presented relative to the electric resistance of the undamaged beam (R_o), i.e., when $a_o = 0$, and crack length, relative to the height of the beam (W). We can observe the same behaviour as it was obtained in previous examples, i.e., the electric resistance increases with the crack length. Moreover, the influence of the piezoresistive behaviour on the electric resistance changes is negligible when compared with the changes caused by the crack.

Finally, Fig. 25 presents the evolution of the electric resistance (R) with the maximum vertical displacement (u_y) at point A, until the objective value $\overline{u}_y$ is reached. Similarly to Fig. 24, the electric resistance is presented relative to the electric resistance of the undamaged beam (R_o). The observed electric resistance evolution in the figure reveals that the crack does not grow monotonously with the deflection of the beam. The constant values for the electric resistance (i.e., the flat regions of the curve) indicates a crack growth arrest zone, whereas the increments on the electric resistance is indicative of a crack growth, so that crack growth can be corelated with the changes in the electrical resistance of the structure.

5. Summary and conclusions

Previous studies illustrate the potential of carbon nanotubes (CNT) as doping nano-additives that can be employed to improve both the mechanical and electrical properties of polymeric materials. In this manner, the mechanical properties (tensile strength, elastic modulus and fracture toughness) of the resulting CNT reinforced composite (CNTRC) may be significantly increased by adding low contents of CNT. Furthermore, the addition of well dispersed CNT to

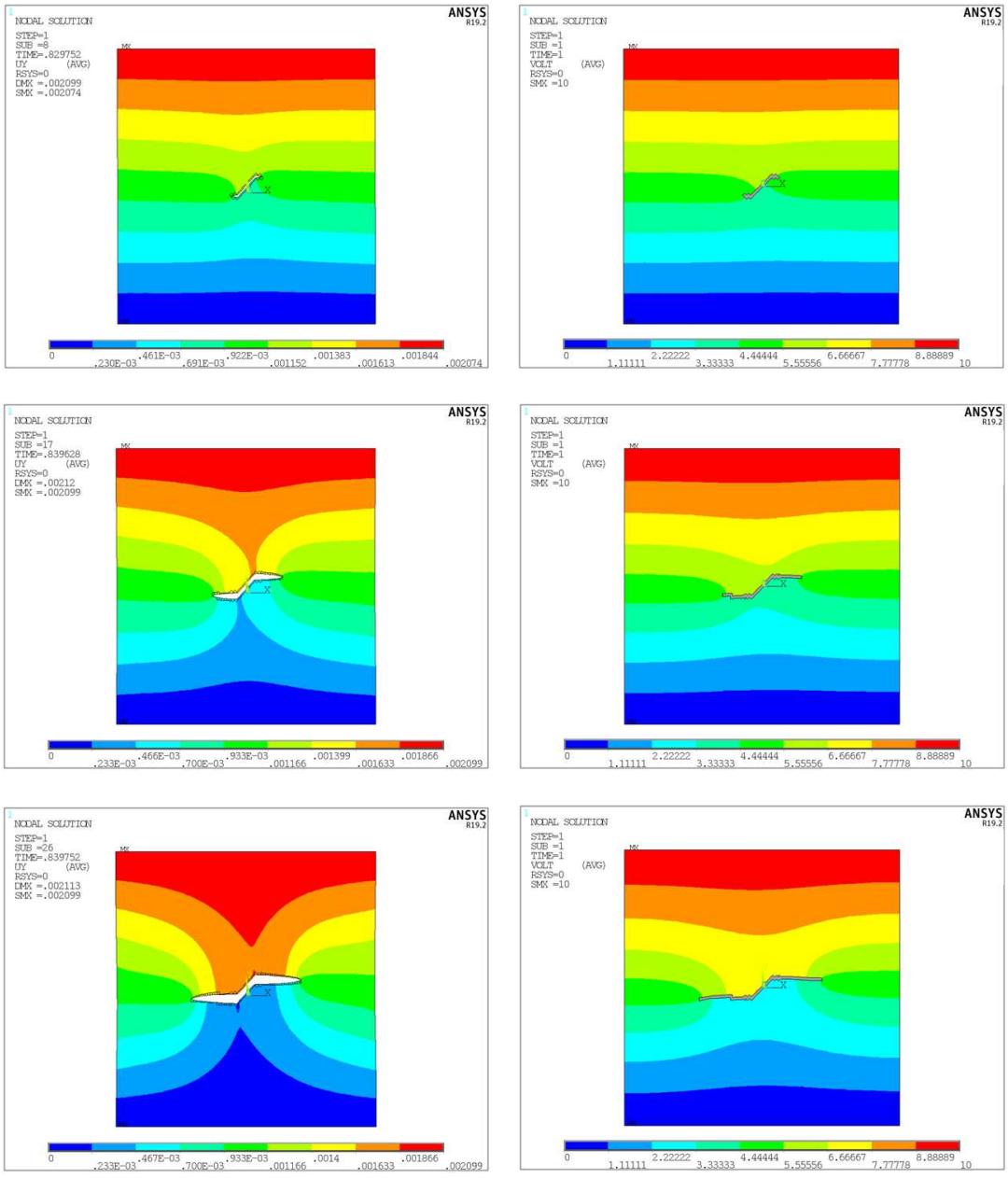

(a) (b)

Figure 20: Influence of an inclined ($\alpha = 45^o$) crack growth evolution on: (a) the vertical displacements (u_y) [m] distribution and (b) the electric potential (ϕ) [V] distribution.

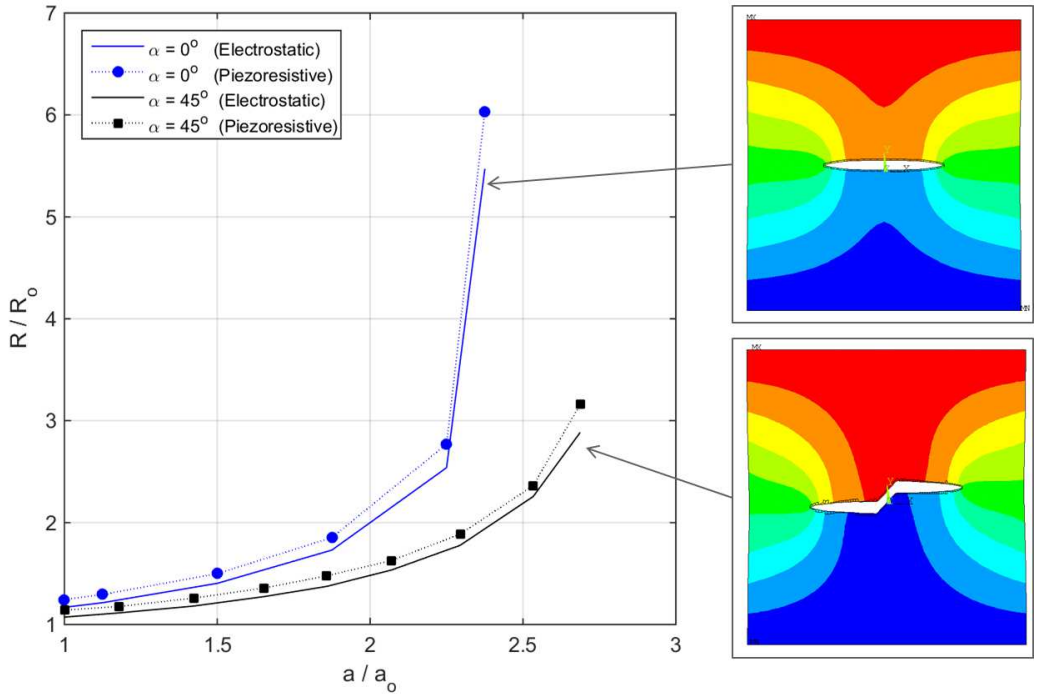

Figure 21: Electric resistance changes caused by a horizontal crack growth (blue lines) and an inclined crack growth (black lines), under piezoresistive (dotted line) and non-piezoresistive (continuous line) conditions.

a certain amount, induces electrical conductivity characteristics in the otherwise non-conductive polymeric matrix. This later property has been exploited to develop self-sensing CNTRC that have the ability to correlate changes in electrical resistivity with modifications in mechanical strain.

In this context, developing numerical tools that assist in estimating the electro-mechanical behavior of these novel materials under the existence of crack-type damage becomes crucial. This paper has presented an XFEM-based numerical framework to simulate how crack-growth affects both the mechanical and electrical behavior of CNTRC materials, that is, how damage affects not only the structural integrity of the component but its self-sensing capability as well.

To this end, the micromechanics model of the electromechanical properties of MWCNT/epoxy nanocomposites, as previously presented by some of the authors in [36], has been first employed to obtain the equivalent (elastic and piezoresistive) properties of the CNTRC. Subsequently, the commercial finite element software ANSYS has been utilized to analyze crack growth by following a two-step scheme:

1) In a first step, the mechanical problem is solved by the XFEM as implemented in ANSYS-, so that the strain state in the cracked domain is computed at each element.

2) The second step implies updating the piezoresistive properties of the elements in terms of the computed strain field (step 1). This results into the definition of a non-homogeneous electrical conductivity problem that, thereafter, is solved using the coupled-field elements available in the ANSYS software.

The proposed numerical scheme has been successfully applied in the paper to analyze several stationary crack and crack-growth configurations. In particular, to characterize how the presence of cracking affects the electric potential field measured in the plates under the electrodes configuration presented in Fig. 7 (b) or Fig. 22 (b). Various parameters have been considered in the analysis, like the electric permeability of the crack, the crack orientation or the severity of the damage, i.e., the crack size. The obtained results reveal that:

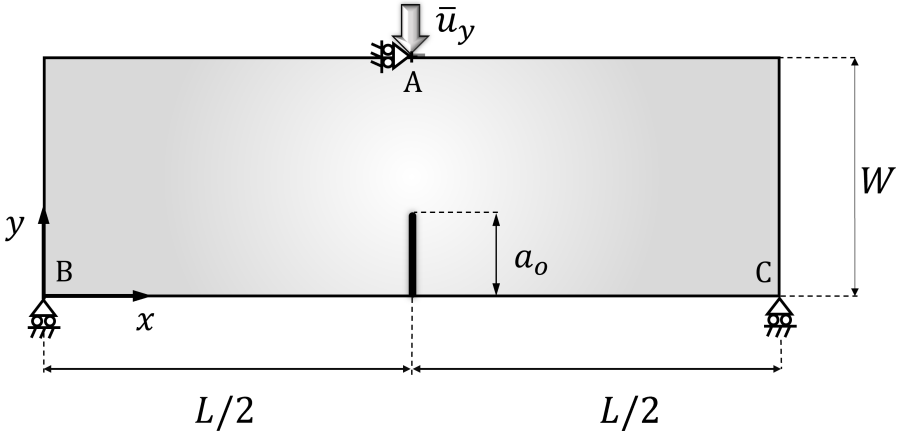

(a)

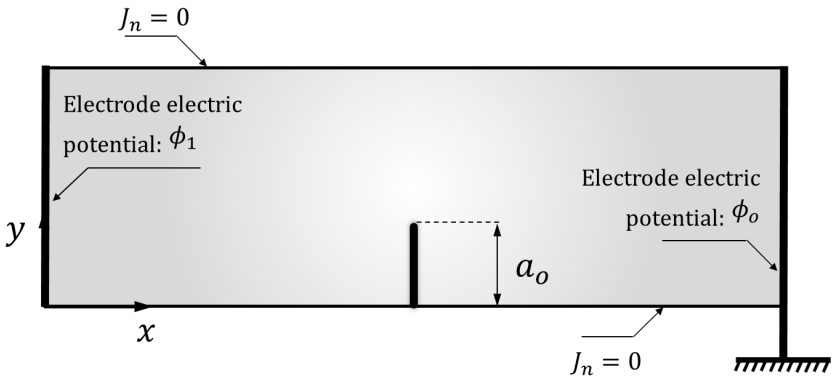

(b)

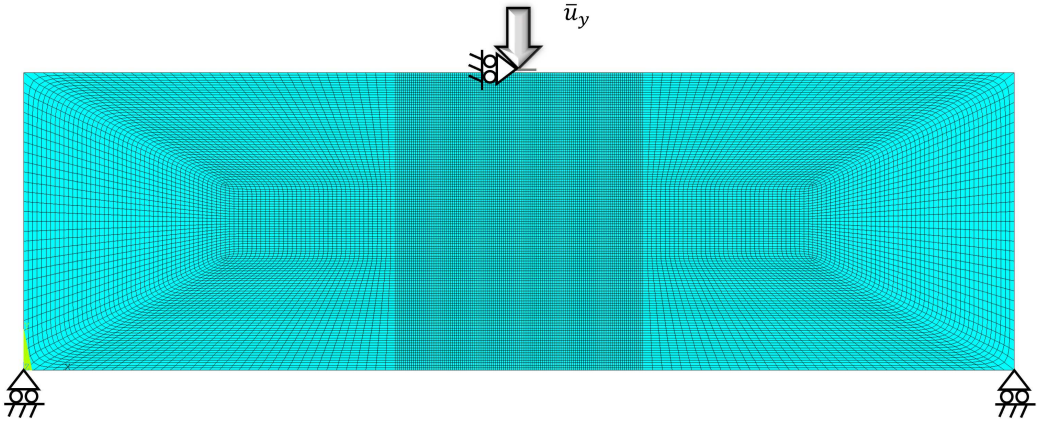

(c)

Figure 22: (a) Three-point flexural test. (b) Electrodes position in the beam. (c) Mesh details.

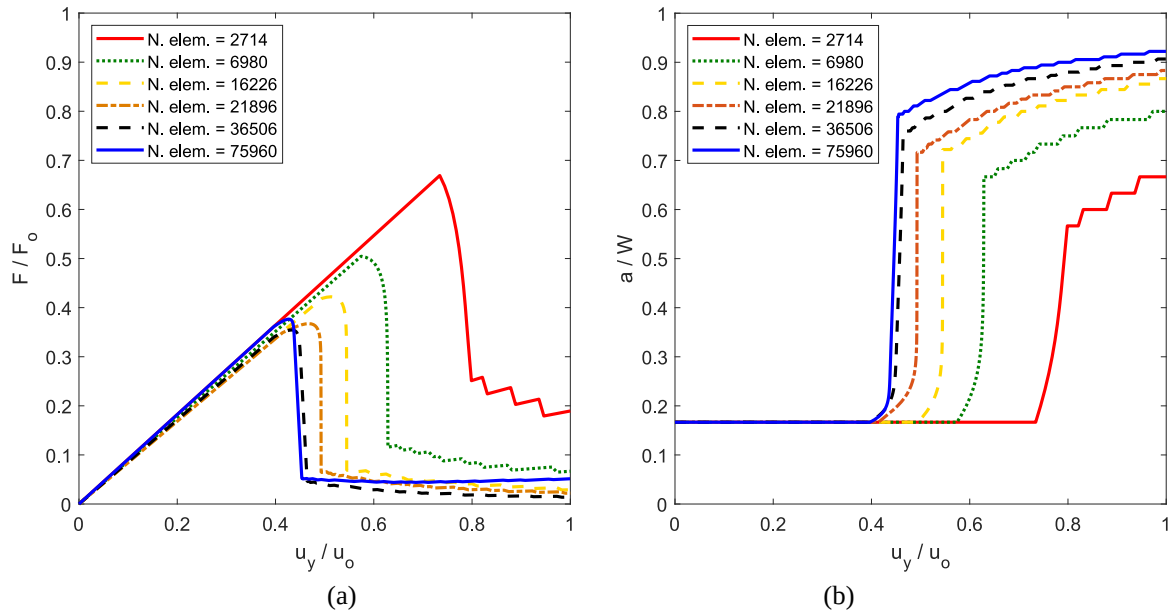

Figure 23: Convergence study on the beam response diagrams: (a) load deflection-curve (i.e., vertical reaction force F/F_o versus the vertical displacement u_y/u_o at $x = L/2$), (b) crack extension a/W versus the maximum deflection of the beam (i.e., u_y/u_o at $x = L/2$).

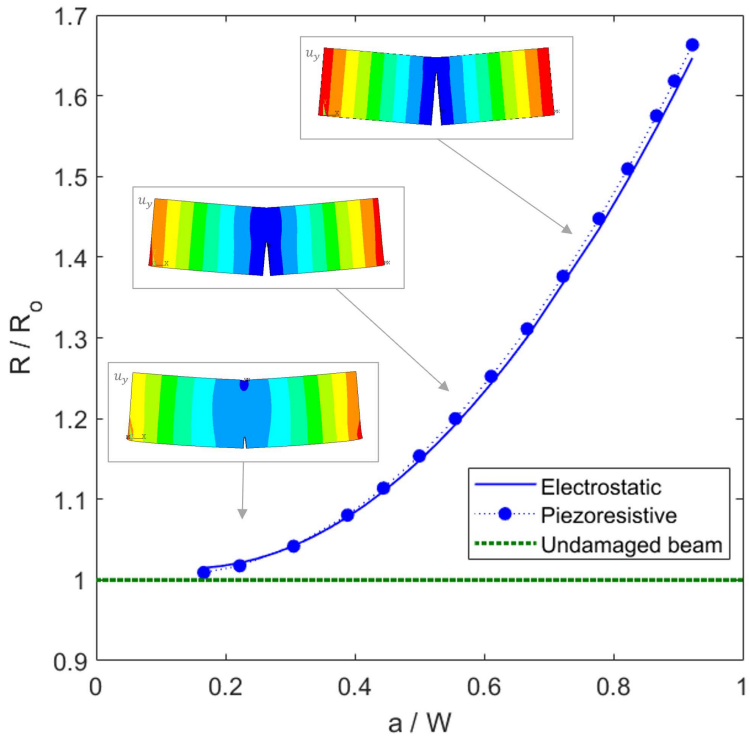

Figure 24: Evolution of the electric resistance (R) with the crack length (a). The electric resistance is presented relative to the electric resistance of the undamaged beam (R_o) and crack length is presented relative to the height of the beam (W).

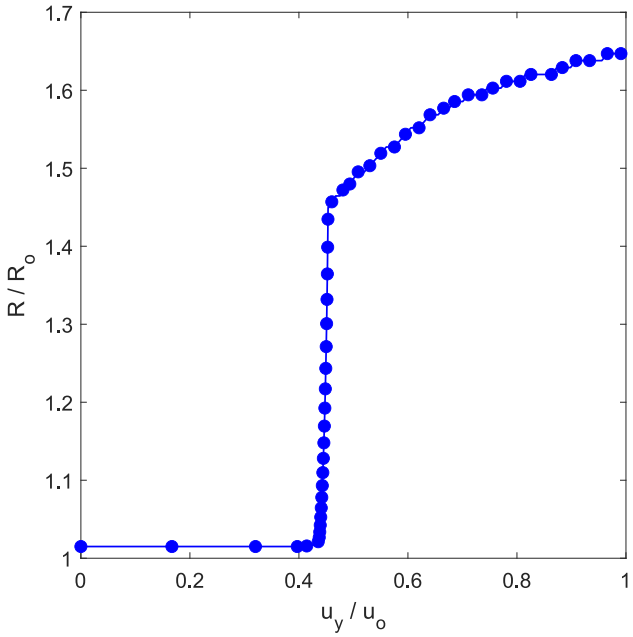

Figure 25: Evolution of the electric resistance (R) with the vertical displacement (u_y) relative to $\bar{u}_y$. The electric resistance is presented relative to the electric resistance of the undamaged beam (R_o), whereas the vertical displacement is presented relative to the vertical displacement imposed at the center of the top edge of the beam ($\bar{u}_y$).

- the lower the crack permittivity is, the better sensor efficiency is observed;
- under electrically impermeable crack-face conditions, the influence of the piezoresistive effect is negligible. This means that the discontinuity induced in the electric field by the presence of the crack surpasses the effect of the change in piezoresistivity provoked by the modification of the strain field due to the crack;
- electric resistance measurements are clearly sensitive to changes in the size and/or the orientation of the crack.

In summary, cracking does not only compromise the mechanical integrity of CNTRC components, but it does also modify their strain self-sensing capabilities. Virtual crack growth monitoring can effectively be conducted by employing the proposed numerical XFEM scheme, in order to further correlate the presence and severity of cracks with the electric resistance measurements in CNTRC plates.

6. Acknowledgments

This work was supported by the *Ministerio de Economía y Competitividad* (Spain) through the research project DPI2017-89162-R and by the *Consejería de Economía, Conocimiento, Empresas y Universidades de la Junta de Andalucía* (Spain) through the research project P18-RT-3128. Both projects were co-funded by the European Regional Development Fund (ERDF). J. Vargas was also supported by a contract-fellowship from the Fondo Social Europeo: Empleo Joven Convocatoria 3/2019, Junta de Andalucía, Ref. EJ3-77.

A. Flowchart scheme

The flowchart scheme of the ANSYS implementation is presented in Fig.26. It should be noted that the three solution steps mentioned in Section 3.3 are underlined in the figure.

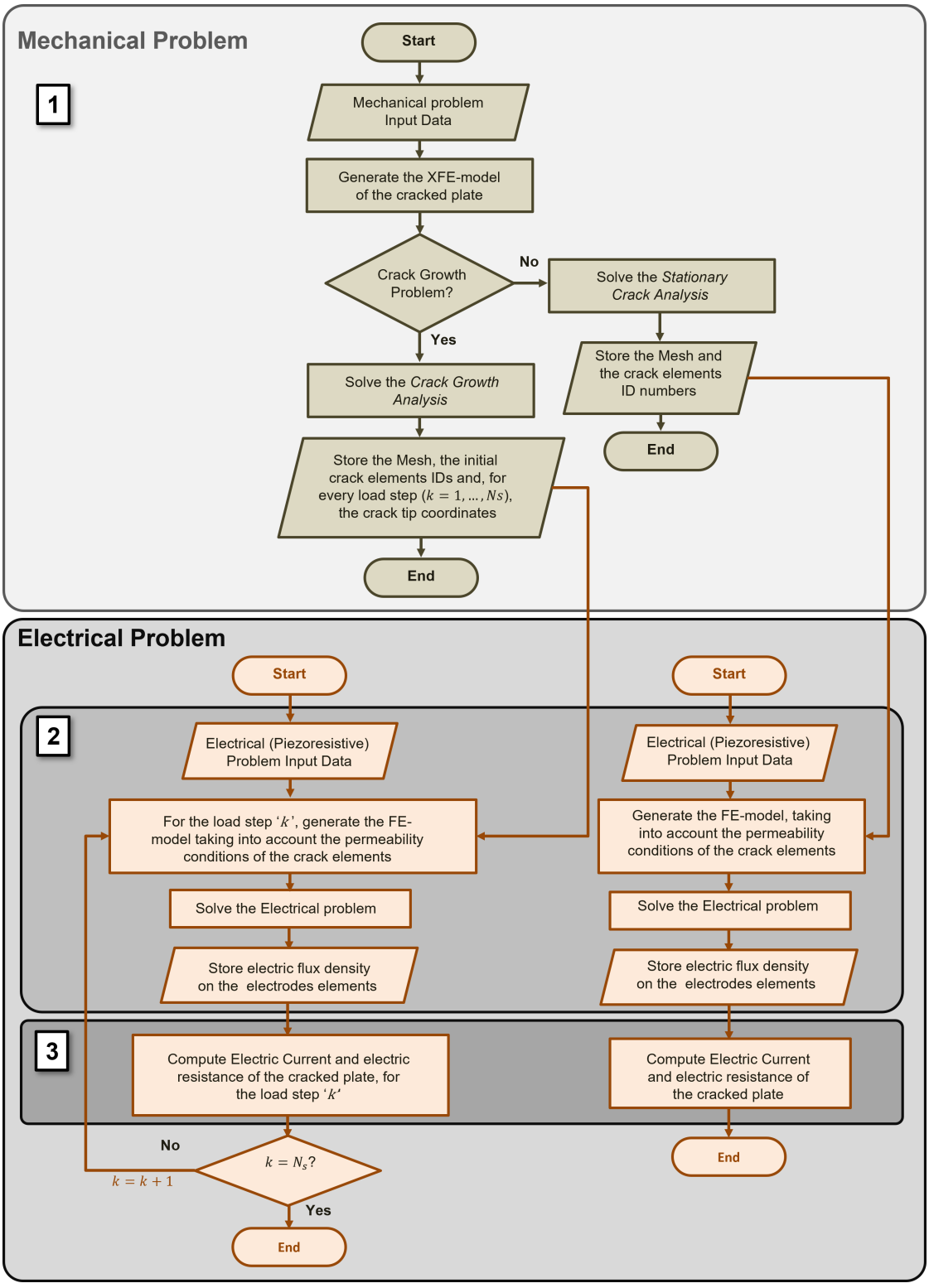

Figure 26: Flowchart scheme with ANSYS.

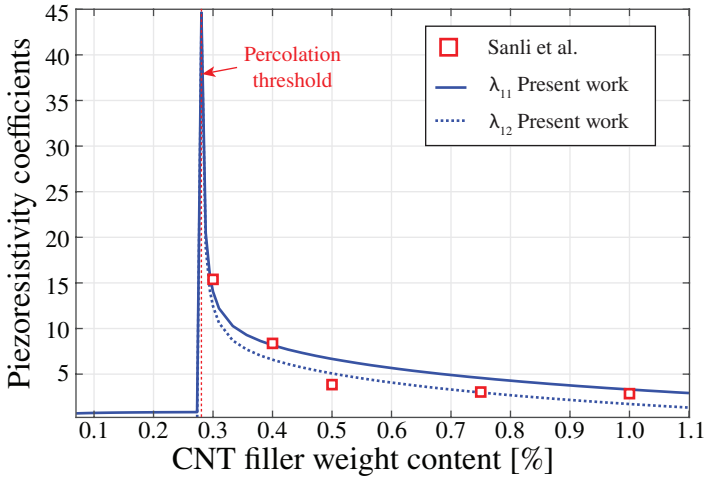

Figure 27: Experimental validation of the adopted micromechanics approach to predict the piezoresistivity coefficients of MWCNT/epoxy composites.

B. Experimental validation of the piezoresistive modeling

In order to demonstrate the accuracy of the micromechanics approach previously introduced in Section 2.3, the theoretical predictions of the piezoresistivity coefficients of MWCNT/epoxy composites are benchmarked against the experimental results reported by Sanli et al. [67] in Fig. 27. Those authors characterized the strain self-sensing properties of dog-bone shaped samples under laterally unconstrained uni-axial stretching (ε_1, $\varepsilon_2 = \varepsilon_3 = -\nu\varepsilon_1$). To do so, the piezoresistivity coefficients were identified as the slope of the linear fitting of the relative variation of the electrical resistance of samples doped with five different CNT contents under quasi-static tensile loading. The electrodes where located perpendicular to the direction of the load, thereby the reported gauge factors correspond to λ_{11} in Eq. (21). In Fig. 27, both the longitudinal λ_{11} and transverse λ_{12} theoretical piezoresistivity coefficients are presented. The model parameters are the same as those used in Section 4. The close agreements between the theoretical and the experimental results for λ_{11} confirm the accuracy of the adopted micromechanics approach. It is observed in this figure that the piezoresistivity coefficients achieve maximum values at filler contents around the percolation threshold ($\approx 0.27\%$). Additionally, it is noted that the transverse piezoresistivity coefficient λ_{12} exhibits slightly higher values than the longitudinal one λ_{11} all along the whole range of filler concentrations.

References

[1] M.F.L. De Volder, S.H. Tawfick, R.H. Baughman, and A.J. Hart. Carbon nanotubes: Present and future commercial applications. *Science*, 339:535–539, 2013.

[2] G. Mittal, V. Dhand, K.Y. Rhee, S.-J. Park, and W.R. Lee. A review on carbon nanotubes and graphene as fillers in reinforced polymer nanocomposites. *Journal of Industrial and Engineering Chemistry*, 21:11–25, 2015.

[3] S. Rathinavel, K. Priyadharshini, and D. Panda. A review on carbon nanotube: An overview of synthesis, properties, functionalization, characterization and the application. *Materials Science and Engineering B: Solid-State Materials for Advanced Technology*, 268:115095, 2021.

[4] K.V. Meena and A. Ravi Sankar. Biomedical catheters with integrated miniature piezoresistive pressure sensors: A review. *IEEE Sensors Journal*, 21:10241–10290, 2021.

[5] A. Iqbal, A. Saeed, and A. Ul-Hamid. A review featuring the fundamentals and advancements of polymer/cnt nanocomposite application in aerospace industry. *Polymer Bulletin*, 78:539–557, 2021.

[6] F.H. Gojny, M.H.G. Wichmann, B. Fiedler , and K. Schulte. Influence of different carbon nanotubes on the mechanical properties of epoxy matrix composites a comparative study. *Compos. Sci. Technol.*, 65:2300–2313, 2005.

[7] T.H. Hsieh, A.J. Kinloch, A.C. Taylor, and I.A. Kinloch. The effect of carbon nanotubes on the fracture toughness and fatigue performance of a thermosetting epoxy polymer. *J. Mater. Sci.*, 46:7525–7535, 2011.

[8] N. Domun, H. Hadavinia, T. Zhang, T. Sainsbury, G.H. Liaghat, and S. Vahid. Improving the fracture toughness and the strength of epoxy using nanomaterials-a review of the current status. *Nanoscale*, 7:10294–10329, 2015.

[9] F.H. Gojny, M.H.G. Wichmann, B. Fiedler, W. Bauhofer, and K. Schulte. Influence of nano-modification on the mechanical and electrical properties of conventional fibre-reinforced composites. *Composites Part A: Applied Science and Manufacturing*, 36:1525–1535, 2005.
[10] W. Bauhofer and J.Z. Kovacs. A review and analysis of electrical percolation in carbon nanotube polymer composites. *Composites Science and Technology*, 69:1486–1498, 2009.
[11] E.T. Thostenson and T.-W. Chou. Real-time in situ sensing of damage evolution in advanced fiber composites using carbon nanotube networks. *Nanotechnology*, 19:215713, 2008.
[12] X. Yu and E. Kwon. A carbon nanotube/cement composite with piezoresistive properties. *Smart Materials and Structures*, 18:055010, 2009.
[13] J. Sebastian, N. Schehl, M. Bouchard, M. Boehle, L. Li, and A. Lagounov K. Lafdi. Health monitoring of structural composites with embedded carbon nanotube coated glass fiber sensors. *Carbon*, 66:191–200, 2014.
[14] S. Luo W. Obitayo and T. Liu. Swcnt-thin-film-enabled fiber sensors for lifelong structural health monitoring of polymeric composites - from manufacturing to utilization to failure. *Carbon*, 76:321–329, 2014.
[15] L. Vertuccio, L. Guadagno, G. Spinelli, P. Lamberti, V. Tucci, and S. Russo. Piezoresistive properties of resin reinforced with carbon nanotubes for health-monitoring of aircraft primary structures. *Composites Part B: Engineering*, 107:192–202, 2016.
[16] A. D'Alessandro, M. Rallini, F. Ubertini, and A.L. Materazzi J.M. Kenny. Investigations on scalable fabrication procedures for self-sensing carbon nanotube cement-matrix composites for shm applications. *Cement and Concrete Composites*, 65:200–213, 2016.
[17] E. García-Macías, L. Rodríguez-Tembleque, A. Sáez, and F. Ubertini. Crack detection and localization in rc beams through smart mwcnt/epoxy strip-like strain sensor. *Smart Materials and Structures*, 27(11):115022, oct 2018.
[18] A. Esmaeili, C. Sbarufatti, D. Ma, A. Manes, A. Jiménez-Suárez, A. Ureña, D. Dellasega, and A.M.S. Hamouda. Strain and crack growth sensing capability of swcnt reinforced epoxy in tensile and mode i fracture tests. *Composites Science and Technology*, 186:107918, 2020.
[19] T. Belytschko and T. Black. Elastic crack growth in finite elements with minimal remeshing. *Int. J. Numer. Methods Eng.*, 46:601–620, 1999.
[20] N. Möes, J. Dolbow, and T. Belytschko. A finite element method for crack growth without remeshing. *Int. J. Numer. Methods Eng.*, 46:131–150, 1999.
[21] N. Sukumar, D. Chopp, N. Moes, and T. Belytschko. Modeling holes and inclusions by level sets in the extended finite-element method. *Comput. Methods Appl. Mech. Eng.*, 190:6183–6200, 2001.
[22] ANSYS, Inc., Cannonsburg, PA. *Fracture Analysis Guide, Release 2019 R1*, 2019.
[23] U.A. Joshi, S.C Sharma, and S.P. Harsha. Analysis of fracture in carbon nanotube based composites using extended finite element method. *Journal of Computational and Theoretical Nanoscience*, 9:872–878, 2012.
[24] M. Eftekhari, S. Hatefi Ardakani, and S. Mohammadi. An xfem multiscale approach for fracture analysis of carbon nanotube reinforced concrete. *Theoretical and Applied Fracture Mechanics*, 72:64–75, 2014.
[25] A.K. Sahoo, I.V. Singh, and B.K. Mishra. Xfem for the evaluation of elastic properties of CNT-based 3-d full five-directional braided composites. *Advanced Composite Materials*, 23:351–373, 2014.
[26] A. Negi, G. Bhardwaj, J.S. Saini, and N. Grover. Crack growth analysis of carbon nanotube reinforced polymer nanocomposite using extended finite element method. *Proceedings of the Institution of Mechanical Engineers, Part C: Journal of Mechanical Engineering Science*, 223:1750–1770, 2019.
[27] A. Negi, G. Bhardwaj, J.S. Saini, K. Khanna, and R.K. Godara. Analysis of cnt reinforced polymer nanocomposite plate in the presence of discontinuities using xfem. *Theoretical and Applied Fracture Mechanics*, 103:102292, 2019.
[28] Z.Y. Liu, K. Ma, G.H. Fan, K. Zhao, J.F. Zhang, B.L. Xiao, and Z.Y. Ma. Enhancement of the strength-ductility relationship for carbon nanotube/alcumg nanocomposites by material parameter optimisation. *Carbon*, 157:602–613, 2020.
[29] S.H. Ebrahimi. Singularity analysis of cracks in hybrid cnt reinforced carbon fiber composites using finite element asymptotic expansion and xfe. *International Journal of Solids and Structures*, 214-215:1–17, 2021.
[30] L. Rodríguez-Tembleque, F. García-Sánchez, E. García-Macías, F.C. Buroni, and A. Sáez. Crack-induced electrical resistivity changes in cracked cnt-reinforced composites. *Theor. Appl. Fract. Mec.*, 106:102470, 2020.
[31] Y. Kuronuma and Y. Shindo and T. Takeda and F. Narita. Fracture behaviour of cracked carbon nanotube-based polymer composites: Experiments and finite element simulations. *Fatigue and Fracture of Engineering Materials and Structures*, 33:87–93, 2010.
[32] Y. Kuronuma and Y. Shindo and T. Takeda and F. Narita. Crack growth characteristics of carbon nanotube-based polymer composites subjected to cyclic loading. *Engineering Fracture Mechanics*, 78:3102–3110, 2011.
[33] Y. Shindo and Y. Kuronuma and T. Takeda and F. Narita and S.-Y. Fu. Electrical resistance change and crack behavior in carbon nanotube/polymer composites under tensile loading. *Composites Part B: Engineering*, 43:39–43, 2012.
[34] T. Takeda and Y. Shindo and F. Naraoka and Y. Kuronuma and F. Narita. Crack and electrical resistance behaviors of carbon nanotube-based polymer composites under mixed-mode i/ii loading. *Materials Transactions*, 54:1105–1109, 2013.
[35] A. Yadav and R.K. Godara and G. Bhardwaj and R.U. Patil and S.K. Singh and K. Khanna. A review on fracture analysis of cnt/graphene reinforced composites for structural application. *Archives of Computational Methods in Engineering*, 54:1105–1109, 2021.
[36] E. García-Macías, R. Castro-Triguero, A. Sáez, and F. Ubertini. 3D mixed micromechanics-FEM modeling of piezoresistive carbon nanotube smart concrete. *Computer Methods in Applied Mechanics and Engineering*, 340:396 – 423, 2018.
[37] F.C. Buroni and E. Garca-Macas. Closed-form solutions for the piezoresistivity properties of short-fiber reinforced composites with percolation-type behavior. *Carbon*, 184:923–940, 2021.
[38] Wenxiang Xu, Fan Wu, Yang Jiao, and Mingjun Liu. A general micromechanical framework of effective moduli for the design of nonspherical nano-and micro-particle reinforced composites with interface properties. *Materials & Design*, 127:162–172, 2017.
[39] Enrique García-Macías, Rafael Castro-Triguero, and Filippo Ubertini. Two-step hierarchical micromechanics model of partially saturated porous composites doped with ellipsoidal particles with interface effects. *Composites Part B: Engineering*, 148:49–60, 2018.
[40] Muneo Hori and Sia Nemat-Nasser. Double-inclusion model and overall moduli of multi-phase composites. *Mechanics of Materials*, 14(3):189–206, 1993.
[41] E. García-Macías, L. Rodríguez, and A. Sáez. MWCNT/epoxy strip-like sensors for buckling detection in beam-like structures. *Thin-Walled Structures*, 133:27 – 41, 2018.
[42] Wenxiang Xu, Huaifa Ma, Shunying Ji, and Huisu Chen. Analytical effective elastic properties of particulate composites with soft interfaces

around anisotropic particles. *Composites Science and Technology*, 129:10–18, 2016.
[43] Toshio Mura. *Micromechanics of defects in solids*, volume 3. Springer Science & Business Media, 1987.
[44] Chuang Feng and Liying Jiang. Micromechanics modeling of the electrical conductivity of carbon nanotube (CNT)–polymer nanocomposites. *Composites Part A: Applied Science and Manufacturing*, 47:143–149, 2013.
[45] Enrique García-Macías, Antonella D'Alessandro, Rafael Castro-Triguero, Domingo Pérez-Mira, and Filippo Ubertini. Micromechanics modeling of the electrical conductivity of carbon nanotube cement-matrix composites. *Composites Part B: Engineering*, 108:451–469, 2017.
[46] John G Simmons. Generalized formula for the electric tunnel effect between similar electrodes separated by a thin insulating film. *Journal of Applied Physics*, 34(6):1793–1803, 1963.
[47] Gary D Seidel and Dimitris C Lagoudas. A micromechanics model for the electrical conductivity of nanotube-polymer nanocomposites. *Journal of Composite Materials*, 43(9):917–941, 2009.
[48] KY Yan, QZ Xue, QB Zheng, and LZ Hao. The interface effect of the effective electrical conductivity of carbon nanotube composites. *Nanotechnology*, 18(25):255705, 2007.
[49] G. M. Odegard and T. S. Gates. Constitutive modeling of nanotube/polymer composites with various nanotube orientation. In *2002 SEM Annual Conference on Experimental and Applied Mechanincs*, 2002.
[50] Fei Deng and Q. S. Zheng. An analytical model of effective electrical conductivity of carbon nanotube composites. *Applied Physics Letters*, 92(7):071902, 2008.
[51] Minoru Taya. *Electronic composites: modeling, characterization, processing, and MEMS applications*. Cambridge University Press, 2005.
[52] C. Feng and L. Y. Jiang. Investigation of uniaxial stretching effects on the electrical conductivity of CNT-polymer nanocomposites. *Journal of Physics D: Applied Physics*, 47(40):405103, 2014.
[53] Takashi Komori and Kunio Makishima. Numbers of fiber-to-fiber contacts in general fiber assemblies. *Textile Research Journal*, 47(1):13–17, 1977.
[54] AP Sobha and Sunil K Narayanankutty. Improved strain sensing property of functionalised multiwalled carbon nanotube/polyaniline composites in TPU matrix. *Sensors and Actuators A: Physical*, 233:98–107, 2015.
[55] F. Erdogan and G. C. Sih. On the crack extension in plates under plane loading and transverse shear. *ASME Journal of Basic Engineering*, 85:519–527, 1963.
[56] M. Ortiz and A. Pandolfi. Finite-deformation irreversible cohesive elements for three-dimensional crack-propagation analysis. *Int. J. Numer. Methods Eng.*, 44:1267–1282, 1999.
[57] N. Möes and T. Belytschko. Extended finite element method for cohesive crack growth. *Eng. Fract. Mech.*, 69:813–833, 2002.
[58] N. Sukumar and J. Prévost. Modeling quasi-static crack growth with the extended finite element method part i: computer implementation. *Int. J. Solids Struct.*, 40:7513–7537, 2003.
[59] T.-P. Fries and T. Belytschko. The extended/generalized finite element method: An overview of the method and its applications. *Int. J. Numer. Methods Eng.*, 84:253–304, 2010.
[60] E. Béchet, M. Scherzer, and M. Kuna. Application of the x-fem to the fracture of piezoelectric materials. *International Journal for Numerical Methods in Engineering*, 77:1535–1565, 2009.
[61] G. Hattori, R. Rojas-Díaz, A. Sáez, N. Sukumar, and F. García-Sánchez. New anisotropic crack-tip enrichment functions for the extended finite element method. *Computational Mechanics*, 50:591–601, 2012.
[62] R. Rojas-Díaz, N. Sukumar, A. Sáez, and F. García-Sánchez. Fracture in magnetoelectroelastic materials using the extended finite element method. *International Journal for Numerical Methods in Engineering*, 88:1238–1259, 2011.
[63] J.H. Song, P.M.A. Areias, and T. Belytschko. A method for dynamic crack and shear band propagation with phantom nodes. *Int. J. Numer. Methods Eng.*, 67:868–893, 2006.
[64] Q. Duan, J.H. Song, T. Menouillard, and T. Belytschko. Element-local level-set method for three-dimensional dynamic crack growth. *Int. J. Numer. Methods Eng.*, 80:1520–1543, 2009.
[65] A. Hansbo and P. Hansbo. A finite element method for the simulation of strong and weak discontinuities in elasticity. *Comput. Methods Appl. Mech. Eng.*, 191:3523–3540, 2004.
[66] J. Mergheim, E. Kuhl, and P. Steinmann. A finite element method for the computational modeling of cohesive cracks. *Int. J. Numer. Methods Eng.*, 63:276–289, 2005.
[67] Abdulkadir Sanli, Christian Mller, Olfa Kanoun, Cagatay Elibol, and Martin F. X. Wagner. Piezoresistive characterization of multi-walled carbon nanotube-epoxy based flexible strain sensitive films by impedance spectroscopy. *Composites Science and Technology*, 122:18–26, 2016.
[68] H. Tada, P.C. Paris, and G.R. Irwin. *The Stress Analysis of Cracks Handbook*. ASME Press, New York, 3rd edition, 2000.